Glu409 (441) and Asn690 (721) are located at the entrance of the ligand-binding cleft in GluK2 (Fig. 6e). Breakage of the hydrogen bond between them was discovered even when an efficacious agonist NDH was bound to GluK2 in this study.

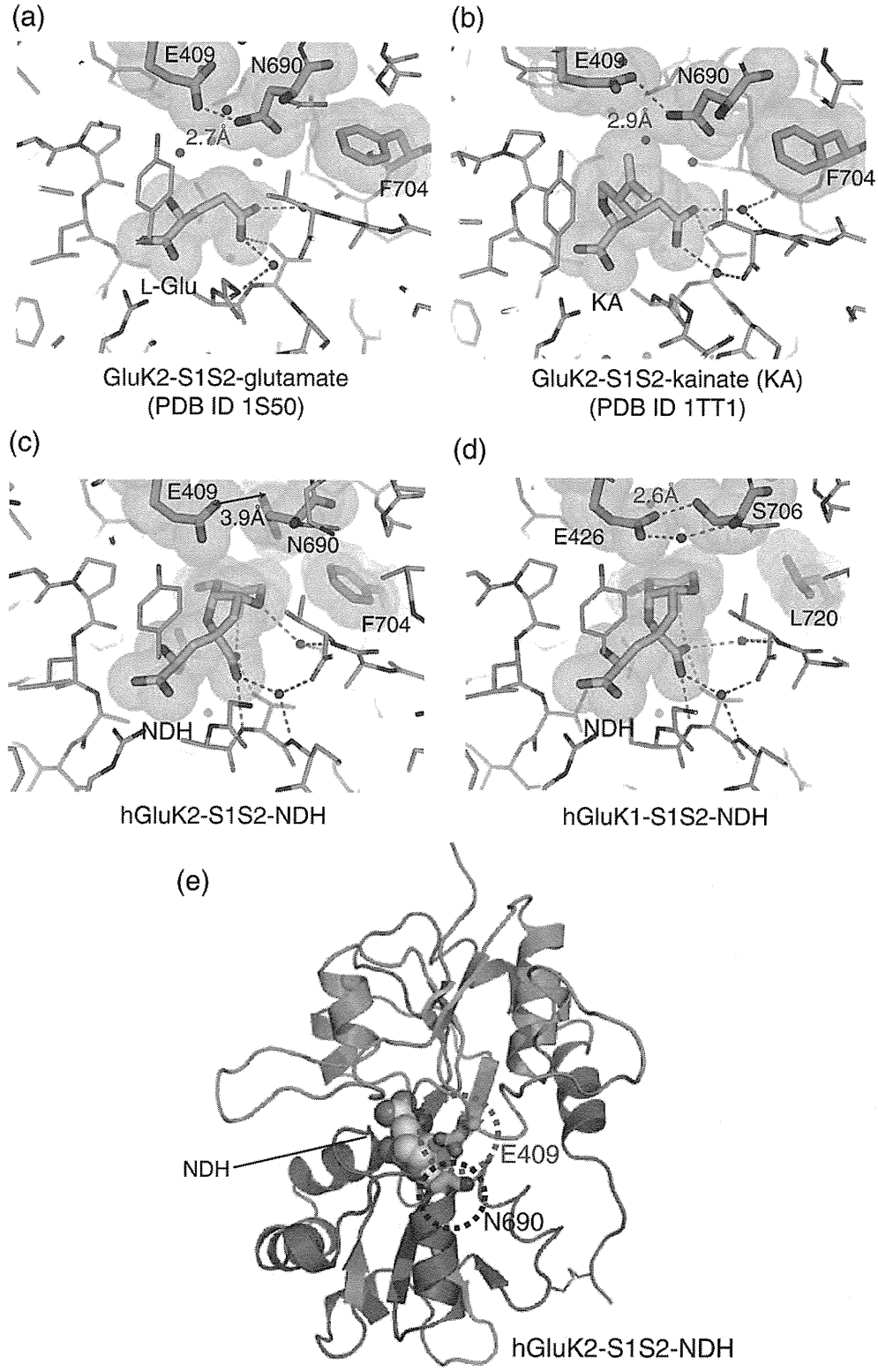

Fig. 6 (*legend on next page*)

Table 3. Distance measurements between domain 1 and domain 2 of hGluK1-S1S2

		Distances (Å)			
		Ser706C$^{\alpha}$–Glu426C$^{\alpha}$	Glu723C$^{\alpha}$–Pro501O	Asp672O–Gly475N	Ser674C$^{\alpha}$–Thr503C$^{\alpha}$
L-glutamate	Molecule A	7.46	8.87	2.89	6.54
	Molecule B	7.24	8.83	2.91	6.54
	Average	7.35	8.85	2.90	6.54
DH	Molecule A	7.55	8.88	2.88	6.49
	Molecule B	7.34	8.93	2.88	6.50
	Average	7.45	8.91	2.88	6.50
NDH	Molecule A	7.52	8.84	2.86	6.53
	Molecule B	7.63	8.87	2.89	6.52
	Average	7.58	8.86	2.87	6.53
MSVIII-19	Molecule A	7.66	8.69	2.89	6.61
	Molecule B	7.60	8.69	2.86	6.58
	Average	7.63	8.69	2.88	6.60
8-deoxy-NDH	Molecule A	7.60	8.74	2.87	6.54
	Molecule B	7.52	8.75	2.86	6.57
	Average	7.56	8.75	2.87	6.56
9-deoxy-NDH	Molecule A	7.61	8.82	2.87	6.58
	Molecule B	7.48	8.79	2.85	6.58
	Average	7.55	8.81	2.86	6.59

Residue pairs were selected in accordance with those in Ref. 26.

Domain closure of hGluK1-S1S2 upon ligand binding

As demonstrated previously for rat GluK1-S1S2,[17] hGluK1-S1S2 showed the induction of full domain closure for DH, NDH and their synthetic analogues. No domain motions were identified by DynDom[25] when compared to the structure of the L-glutamate complex obtained under similar crystallization conditions. Distances between the centers of masses for domains 1 and 2 were very similar (23.82, 23.65, 23.76, 23.92, 23.82 and 23.85 Å for L-glutamate, DH, NDH, MSVIII-19, 8-deoxy-NDH and 9-deoxy-NDH complexes, respectively). In order to compare the previous MD simulation by Postila *et al.*,[26] we also measured the distances between selected atom pairs reflecting to cleft opening (Table 3). In the crystal structures, none of the ligands induced cleft opening. Hydrogen-bonding interactions between Asp672 (687)N and Gly475 (490)O and the side chains of Glu426 (441) and Ser706 (721)[26] were maintained in all structures.

In the previous study, DH, NDH and 8-deoxy-NDH were characterized as full or relatively efficacious agonists for GluK1, and 9-deoxy-NDH was shown to be a partial agonist with low efficacy, while MSVIII-19 was a potential antagonist.[11,12,16,23] Thus, the present results clearly indicate that, in DH analogues, induction of domain closure does not correlate directly with their agonist efficacy for GluK1 as has been suggested earlier by Frydenvang *et al.*[17]

Since the "twist" motion of the bottom lobe relative to the upper lobe of the ligand-binding core was recently proposed as being one of the factors that affect agonist efficacy in the AMPA receptors,[27] we compared the structures of the L-glutamate complex and a series of DH analogue complexes. At first, we superposed each ligand complex structure to the L-glutamate complex. Then we determined the principal axis and the vertical axis as described in a structural study for AMPA receptors (Fig. 7a). Vector from the center of mass of domain 2 to that of domain 1 was calculated for each ligand complex, then the L-glutamate complex vector was subtracted from the ligand complex vector (Fig. 7b). The twist motion between the two domains would be indicated by offset from the center in the graph. However, the maximum displacement was 0.3 Å; this value was not significantly larger compared to the crystallographic error range at 1.5 Å resolution.

Fig. 6. Conformations of Asn690 (721) in GluK2 and the corresponding residue Ser706 (721) in GluK1. (a) GluK2-S1S2–L-glutamate complex (PDB ID 1S50), (b) GluK2-S1S2–kainate complex (PDB ID 1TT1) and (c) hGluK2-S1S2–NDH complex. In the NDH complex, Asn690 (721) is toward the opposite side of the bound ligand only in the NDH complex. Asn690 (721) formed a hydrogen bond to Glu409 (441) in the L-glutamate and the KA complex, but the hydrogen bond was disrupted in the NDH complex. (d) hGluK1-S1S2–NDH complex. Residues Glu409 (441), Asn690 (721) and Phe704 (735) in GluK2; Glu426 (441), Asn706 (721) and Leu720 (735) in GluK1; and ligands have been encircled by a transparent van der Waals sphere. (e) Overall structure of hGluK2-S1S2 and positions of Glu409 (441) and Asn690 (721). S1 and S2 segments are represented as green and magenta, respectively. NDH is depicted by the CPK model (C, N and O atoms are represented as yellow, blue and red, respectively). Glu409 (441) and Asn690 (721) are highlighted with stick representation (cyan-based).

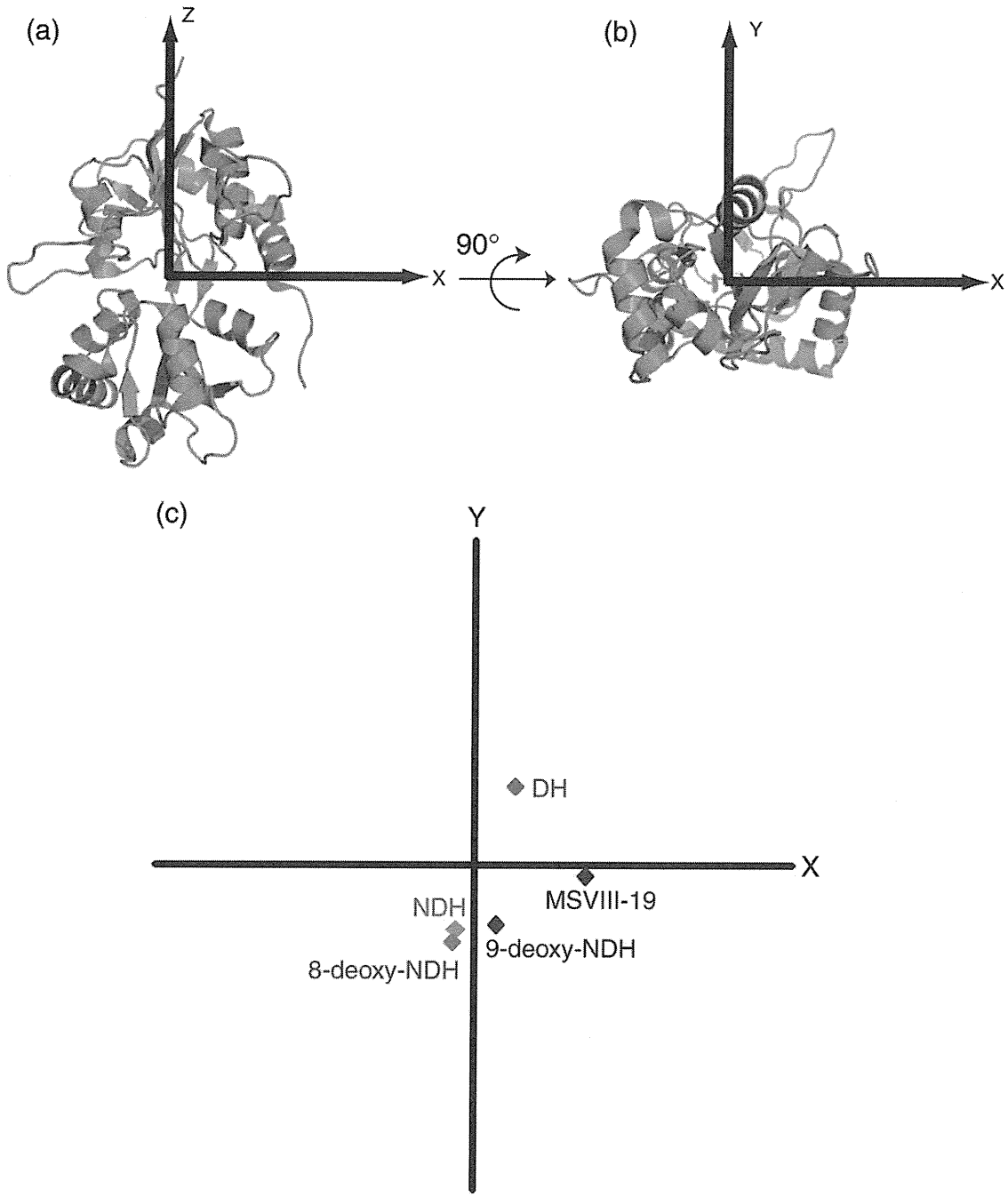

Fig. 7. Principle-axis analysis does not show significant conformational responses of hGluK1-S1S2 in binding ligands. (a and b) The structure of hGluK1-S1S2 was aligned to its principal axes as shown in face (a) and bottom (b) views of the domain. (c) To visualize twist motion associated with ligand binding, we show the center-of-mass displacements of domain 2. Colored marks represent the end points of vectors from the center of mass of domain 2 to the center of mass of domain 1 of the ligand complex subtracted by the corresponding vectors for the L-glutamate complex. Red, DH; orange, NDH; blue, MSVIII-19; green, 8-deoxy-NDH; purple, 9-deoxy-NDH.

Discussion

DH and NDH are naturally occurring amino acids that bind strongly to GluK1 and GluK2. Their synthetic analogues, 8-deoxy-NDH, 9-deoxy-NDH and MSVIII-19, exhibit a wide range of binding potency and agonist efficacy (Table 1). In the present study, we determined the structures of hGluK1-S1S2 in complex with six different ligands: L-glutamate, DH, NDH, MSVIII-19, 8-deoxy-NDH

and 9-deoxy-NDH. We also determined the structure of hGluK2-S1S2 in complex with NDH. The structures of rat GluK1-S1S2 complexed with L-glutamate, DH and MSVIII-19 and the structure of rat GluK2-S1S2 complexed with L-glutamate have been reported previously.[17,21,22] Results generated during the present study provided us with an opportunity to investigate the structural basis of binding and function in important agonists, DH analogues, for GluK1 and GluK2.

The first and most obvious question to consider was whether observed differences between rat and human receptors reflect any structural changes within agonist–receptor complexes, as the only difference between these receptors is a three-amino-acid sequence in the ligand-binding core (Supporting Information and Fig. S4; UniProtKB P22756 and P39086 for rat and human sequences, respectively). As expected, our present results confirmed the close similarity in structure and ligand-binding mode between the human and the rat receptor–ligand complexes. However, we also observed several differences including loop orientation between helices G and H, where 2 out of 10 amino acids differ between human and rat (Fig. 2e). We also noted two different conformations for Tyr429 (444) in the human DH complex, although no such variation has been reported for the other complexes. However, the physiological importance of these differences remains unclear.

Our data provided several interesting implications for binding mode between DH analogues and GluK1 and GluK2. Previous results indicated that removal of the C_8 hydroxy group of NDH drastically reduced affinity for GluK2 while maintaining affinity for GluK1. Furthermore, deletion of the C_9 hydroxy group prevents ligands from binding to GluK2. Such properties are fundamental to the binding selectivity of the ligands for GluK1 and GluK2 (Table 1).[11] These data raised the question of why apparently smaller analogues lose affinity to GluK2, even though the volume of the binding pocket for GluK2 was smaller than that of GluK1?[21] This point has been discussed previously by Lash *et al.* on the basis of MD simulation.[11] Since the present study provides the first experimental evidence to show atomic interactions between GluK2 and NDH, we had the opportunity to address general aspects of binding mode. As proposed earlier, the C_8 and C_9 hydroxy groups are important in that they form hydrogen bonds with key residues in the ligand-binding core. Our data suggested, however, that the contribution of the C_8 hydroxy group to the stability of GluK1 and GluK2 complexes was clearly different. The C_8 hydroxy group in GluK2 had two hydrogen bonds with Glu707 (738) and Thr710 (741), whereas that in GluK1 only formed one hydrogen bond with Glu723 (738) (Table 2). Interestingly, no hydrogen-bonding interaction was detected between the C_8 hydroxy group of NDH and the Ser726 (741) residue in GluK1 that corresponds to Thr710 (741) in GluK2. This subtle difference was not predicted by MD simulation.[11,17]

Another interesting aspect in ligand binding between GluK2 resides in the orientation of Asn690 (721). Previously, Asn690 (721) was demonstrated to be a key residue that interferes with the binding of GluK1-selective ligands to GluK2 by steric occlusion.[17,21,28–30] Our crystal structure largely agreed with earlier predictions. However, a drastic rotation of the Asn690 (721) residue of GluK2 found in the crystal structure permitted NDH to enter the ligand-binding cavity. This conformational change disrupted important interdomain hydrogen bonding between Glu409 (441) and Asn690 (721), similar to that predicted for the GluK2-S1S2–MSVIII-19 complex.[17] This was unexpected because NDH functions as an efficacious agonist, and a firm hydrogen-bonding interaction between Glu409 (441) and Asn690 (721) was previously identified as an important determinant for a positive relationship between channel opening and domain closure.[17] Thus, the crystal structure of the hGluK2-S1S2–NDH complex suggested that, in GluK2, both domain closure and interdomain hydrogen bonding between Glu409 (441) and Asn690 (721) were not simply a determinant of the degree of channel opening. Smaller ligands, such as L-glutamate and kainate, did not induce this conformational change in Asn690 (721).[21]

In the present study, we found that deletion of the NDH C_9 hydroxy group caused conformational change in the associated ligand in binding complex with GluK1. 9-Deoxy-NDH was discovered in the twisted-boat form as a dominant conformation. This conformational change was attributed to the loss of an intramolecular hydrogen bond between the C_9 hydroxy group and the γ-carboxylate of the glutamate substructure in NDH (Fig. 4). This conformational change causes some loss of interactions within the GluK1 ligand-binding pocket, which reduce binding affinity for GluK1. However, lack of the steric occlusion by Asn690 (721), which was observed in GluK2, probably allowed binding of 9-deoxy-NDH with the twisted-boat form or of MSVIII-19 in a flattened conformation to GluK1. Moreover, approximately 10 hydrogen bonds formed tightly between GluK1 and the glutamate substructure can compensate for reduced affinity in the bicyclic portion. In contrast, these compounds are geometrically unfavorable for packing into GluK2-binding cavity unless Asn690 (721) is rotated. These observations concur with earlier findings.[11,17] In the crystal structure of the 9-deoxy-NDH complex, we observed the presence of a minor conformer in the extended bicyclic conformation, similar to MSVIII-19. It can thus be speculated that difference in ligand efficacy between 9-deoxy-NDH and

MSVIII-19 may underlie these structural differences; that is, if all 9-deoxy-NDH existed as only the "extended" conformation, then it would act as functional antagonist like MSVIII-19.

We also found that all of the NDH analogues investigated herein induced full domain closure, regardless of binding potency and agonist efficacy. This finding is consistent with the previously reported structures of DH and MSVIII-19 complexes.[17] It, however, differs with the observation in the domoate and kainate complexes with GluK2 where those partial agonists did not induce complete closure of the receptor.[31] Recently, twist motion between domain 1 and domain 2 was proposed as a factor that modulates channel opening efficacy upon ligand binding in GluA2.[27] Since Frydenvang *et al.* suggested additional factors underlying in the regulation of agonist efficacy in KAR,[17] we examined a series of ligand-bound GluK1 obtained in the present study for "twist" motion. Although slight differences in the motion between domain 1 and domain 2 relative to that of L-glutamate were detected, they were within the atomic resolution of the structure (Fig. 7). We therefore conclude that no significant twist motions exist when DH analogues bind to KAR ligand-binding core. This observation may suggest the following possibilities: (1) twist motion is not a factor that affects the agonist efficacy of DH for GluK1, and thus, some other mechanisms that govern the gating efficacy exist; (2) since DH stabilizes the desensitized state of the receptor so effectively, the crystal structures we obtained represent only a "snapshot" of the most stable ligand–receptor complex. Therefore, the "twist" motion may be still a possible factor, but it was not revealed in the crystal structures. Co-crystallization of DH analogues with non-desensitizing mutants of GluK1 would be necessary to clarify whether or not the motion of ligand-binding core is a factor for activating the channel.

Materials and Methods

DH analogues

DH and NDH were isolated from the marine sponge *L. chondrodes* as previously described by Sakai *et al.*[3,5] DH analogues, 8-deoxy-NDH, 9-deoxy-NDH and MSVIII-19, were synthesized as previously described.[7]

Protein expression

Constructs for expressing hGluK1-S1S2 and hGluK2-S1S2 were engineered in accordance with a procedure described previously.[22] S1 (415-ANRTL-ILYRK-529) and S2 (652-PIDSA-GNGCP-790) segments constituting that of hGluK1-S1S2 were amplified by polymerase chain reaction (PCR) from cDNA (human brain whole marathon ready; Clontech) using the following primers: S1-forward, ATTTGAATTCCGTGGTGCCAACAGAACACTCATTG; S1-reverse, ATTAGGTACCCTTCCGGTAGAGAATGC; S2-forward, ATTAGGTACCCCCATAGATTCGGCAGATG; and S2-reverse, AATTCTCGAGTTAGGGGCAGCCATTCCCA. Similarly, S1 (398-SNRSL-ILYRK-513) and S2 (636-PIDSA-NGCPE-775) segments constituting that of hGluK2-S1S2 were PCR amplified using the following primers: S1-forward, ACAGATGCTAGCTCCAATCGTTCTTTGATT; S1-reverse, TGTACCGGTACCCTTGCGGTACAAAATAC; S2-forward, CGCATGGGTACCCCTATTGACTCTGCTGAT; and S2-reverse, CTCTTTCTCGAGTTATTCTGGGCAACCATTG. PCR products were digested with EcoRI for the region corresponding to the hGluK1 N-terminus of S1 (NheI for hGluK2), with KpnI for regions corresponding to both the C-terminus of S1 and the N-terminus of S2 and with XhoI for the region corresponding to the C-terminus of S2, respectively. The digested insert was extracted and ligated with the pCold I DNA vector (TAKARA), which had been previously digested with EcoRI and SalI, since the pCold I DNA lacked a XhoI site. hGluK1-S1S2 was co-expressed with GroEL/ES using BL21(DE3) cells transformed by the chaperon plasmid pGro7 at 15 °C. Protein was successfully obtained from the supernatant after cell harvesting and centrifugation. Active hGluK2-S1S2 was successfully obtained only by co-expression with molecular chaperon. The sequences of the insert DNAs were verified by sequencing, and the expressed proteins were verified by matrix-assisted laser desorption/ionization–time of flight mass spectrometry. Expressed hGluK1-S1S2 and hGluK2-S1S2 sequences are numbered with respect to the first amino acid in the mature proteins.[21]

Protein purification

hGluK1-S1S2 was purified using an SP Sepharose high-performance (GE Healthcare) cation exchanger column with a linear gradient of 0–500 mM NaCl in 20 mM sodium phosphate buffer, pH 7.4. Following dialysis against 20 mM sodium phosphate buffer (pH 7.4), the protein was further purified by Ni^{2+} affinity chromatography using Ni-NTA agarose (QIAGEN) with a linear gradient of 0–500 mM imidazole in 20 mM Tris–HCl, pH 7.4. After dialysis against 20 mM Tris–HCl (pH 7.4), the His-tag was cleaved off by adding trypsin to the solution so that the weight ratio of trypsin to proteins was 1500, and the solution was maintained at room temperature for 80 min. The reaction was stopped by adding phenylmethylsulfonyl fluoride (1.3 mM) and ethylenediaminetetraacetic acid (EDTA) (20 mM). hGluK1-S1S2 was further purified using SP Sepharose high performance and Ni-NTA agarose, from which the flow-through fraction was collected for crystallization.

hGluK2-S1S2 was purified by a procedure similar to that for hGluK1-S1S2. However, in this case, the purification buffer contained 1 mM sodium hydrogen L-glutamate monohydrate, and thrombin was used instead of trypsin for His-tag digestion.

Crystallization

C2 crystals were obtained for complexes with L-glutamate, DH and NDH. Protein (5–15 mg/mL) was

dialyzed against a buffer containing 20 mM Hepes (pH 7.0), 30 mM NaCl and 1.0 mM EDTA. Crystals were obtained at 6 °C in hanging drops containing 2 μL protein and 2 μL reservoir solution, consisting of 13–23% polyethylene glycol (PEG) 3350, 10 mM citrate (pH 4.8), 1.0 M β-mercaptoethanol and 1–10 mM ligands (L-glutamate, DH or NDH). Crystals were grown for 5 days. Crystals were then transferred through a cryoprotectant with 18% glycerol in reservoir solution prior to flash-cooling in a cold nitrogen stream. *P*1 crystals were obtained for all ligand complexes reported herein. For crystallization, protein was concentrated to 2–3 mg/mL in a buffer containing 20 mM Hepes (pH 7.0), 30 mM NaCl and 1.0 mM EDTA. Crystals were obtained at 30 °C in hanging drops containing 2 μL protein solution and 2 μL reservoir solution, consisting of 25% PEG 3350, 0.3 M Li_2SO_4, 0.2 M 2-[bis(2-hydroxyethyl)amino]-2-(hydroxymethyl)propane-1,3-diol (pH 5.5) and 2–30 mM ligands. Only for the MSVIII-19 complex crystals, 1 mM aspartic acid was added to the reservoir solution.

In order to crystallize hGluK2-S1S2 in complex with NDH, the protein was concentrated to 5–15 mg/mL in a buffer containing 2 mM Tris–HCl (pH 8.0), 20 mM NaCl, 1.0 mM EDTA and 10 mM sodium L-aspartate monohydrate. Crystals were obtained at 30 °C in hanging drops containing 2 μL protein solution and 2 μL reservoir solution, consisting of 40% PEG 4000, 1 mM EDTA, 10 mM NaCl, 2 mM Tris, 1.25 mM glutathione, 1.25 mM glutathione disulfide and 50–300 mM NDH adjusted to pH 4.6.

Data collection

X-ray diffraction data were collected at 100 K using an oscillation method (1.0° per frame) in synchrotron facilities using beamlines, detectors, camera distance, exposure time per frame and wavelength listed in Table S1. Data for BL26B1 and BL26B2 were obtained using mail-in service. The HKL-2000 package[32] was used for auto-indexing and data processing. For statistics, see Table S1.

Structure determinations and refinements

The L-glutamate complex of the hGluK1-S1S2 structure (type I) was first determined by the molecular replacement method using the *CNS* program package.[33,34] The structure of the rat GluK1-S1S2 (GluR5-S1S2) in complex with L-glutamate (PDB ID 1txf)[21] was used as a search model, from which L-glutamate and water molecules were omitted. Manual model building and correction were performed with the program Coot.[35] Initial model refinements and calculations were carried out with the *CNS* program with iterative cycles of simulated annealing and individual *B*-factor refinements. After several refinement cycles, water molecules, SO_4^{2-} ions, β-mercaptoethanol and L-glutamate were added to the model. The model was further refined using the maximum-likelihood target with the program REFMAC5.[36] After the introduction of alternative conformations for several residues and the translation–liberation–screw refinement,[37] the final *R* and R_{free} factors dropped to 20.1% and 24.5%, respectively.

The structure of the hGluK1-S1S2–L-glutamate complex was used as a search model in order to determine the structures of DH and NDH complexes (in *C*2 crystals). These structures were refined using the same procedure as that performed for the L-glutamate complex. Molecular structures of the ligands and the dictionaries used for successive calculations were produced by the PRODRG server.[38] Model reconstruction of the compounds were carried out with TURBO-FRODO.[39]

Structures of the complexes with the DH analogues and the L-glutamate complex in the *P*1 s.g. were determined by the molecular replacement method using the DH complex of the hGluK1-S1S2 structure as a search model. All *P*1 crystals contained two molecules of hGluK1-S1S2 in the a. u. After determining the initial phase, structures were refined by the same procedure. The C-terminal region between Arg785 (800) and Gly788 (803) was disordered; thus, only main chains were modeled [Cys789 (804) and Pro790 (805) were unambiguously determined].

Finally, the NDH complex of the hGluK2-S1S2 structure was determined by the molecular replacement method using the structure of the rat GluK2-S1S2 (GluR6-S1S2) in complex with L-glutamate (PDB ID 3g3f) as the initial model. The structure was refined using the same procedure. Refinement statistics are listed in Table S1.

Accession numbers

Coordinates of hGluK1-S1S2 have been submitted to the PDB [2ZNS for the L-glutamate complex (s.g. *C*2), 2ZNT for the DH complex (s.g. *C*2), 2ZNU for the NDH complex (s.g. *C*2), 3FUZ for the L-glutamate complex (s.g. *P*1), 3FV1 for the DH complex (s.g. *P*1), 3FV2 for the NDH complex (s.g. *P*1), 3FVG for the MSVIII-19 complex, 3FVK for the 8-deoxy-NDH complex and 3FVN for the 9-deoxy-NDH complex of GluK1-S1S2]. Coordinates of hGluK2-S1S2 in complex with NDH is submitted as 3QXM.

Acknowledgements

This work has been supported in part by a project grant from the Institute of Multidisciplinary Research for Advanced Material, Tohoku University (to M.U.); the Management Expenses Grants for National Universities Corporations (to M.I.-S.) from Ministry of Education, Culture, Sports, Science and Technology, Japan; and Grants-in-Aid for Scientific Research 20770076, 18032012 (to M.U.) and 16073202 (to M.S.) from Japan Society for the Promotion of Science and Ministry of Education, Culture, Sports, Science and Technology, Japan. Synchrotron radiation experiments were performed at BL44B2, BL26B1 and BL26B2 (RIKEN beamlines) of SPring-8 and at BL5A, BL17A, NE3A and NW12A of Photon Factory and Photon Factory Advanced Ring under the approval of 2007G515, 2007G516 and 2009G501.

Supplementary Data

Supplementary data to this article can be found online at doi:10.1016/j.jmb.2011.08.043

References

1. Hollmann, M. & Heinemann, S. (1994). Cloned glutamate receptors. *Annu. Rev. Neurosci.* **17**, 31–108.
2. Swanson, G. T. & Sakai, R. (2009). Ligands for ionotropic glutamate receptors. *Prog. Mol. Subcell. Biol.* **46**, 123–157.
3. Sakai, R., Kamiya, H., Murata, M. & Shimamoto, K. (1997). Dysiherbaine: a new neurotoxic amino acid from the Micronesian marine sponge *Dysidea herbacea*. *J. Am. Chem. Soc.* **119**, 4112–4116.
4. Sakai, R., Swanson, G. T., Shimamoto, K., Green, T., Contractor, A., Ghetti, A. *et al.* (2001). Pharmacological properties of the potent epileptogenic amino acid dysiherbaine, a novel glutamate receptor agonist isolated from the marine sponge *Dysidea herbacea*. *J. Pharmacol. Exp. Ther.* **296**, 650–658.
5. Sakai, R., Koike, T., Sasaki, M., Shimamoto, K., Oiwa, C., Yano, A. *et al.* (2001). Isolation, structure determination, and synthesis of neodysiherbaine A, a new excitatory amino acid from a marine sponge. *Org. Lett.* **3**, 1479–1482.
6. Swanson, G. T., Green, T., Sakai, R., Contractor, A., Che, W., Kamiya, H. & Heinemann, S. F. (2002). Differential activation of individual subunits in heteromeric kainate receptors. *Neuron*, **34**, 589–598.
7. Shoji, M., Akiyama, N., Tsubone, K., Lash, L. L., Sanders, J. M., Swanson, G. T. *et al.* (2006). Total synthesis and biological evaluation of neodysiherbaine A and analogues. *J. Org. Chem.* **71**, 5208–5220.
8. Sasaki, M., Tsubone, K., Shoji, M., Oikawa, M., Shimamoto, K. & Sakai, R. (2006). Design, total synthesis, and biological evaluation of neodysiherbaine A derivative as potential probes. *Bioorg. Med. Chem. Lett.* **16**, 5784–5787.
9. Sakai, R., Swanson, G. T., Sasaki, M., Shimamoto, K. & Kamiya, H. (2006). Dysiherbaine: a new generation of excitatory amino acids of marine origin. *Cent. Nerv. Syst. Agents Med. Chem.* **6**, 83–108.
10. Sasaki, M., Tsubone, K., Aoki, K., Akiyama, N., Shoji, M., Oikawa, M. *et al.* (2008). Rapid and efficient synthesis of dysiherbaine and analogues to explore structure–activity relationships. *J. Org. Chem.* **73**, 264–273.
11. Lash, L. L., Sanders, J. M., Akiyama, N., Shoji, M., Postila, P., Pentikainen, O. T. *et al.* (2008). Novel analogs and stereoisomers of the marine toxin neodysiherbaine with specificity for kainate receptors. *J. Pharmacol. Exp. Ther.* **324**, 484–496.
12. Sanders, J. M., Ito, K., Settimo, L., Pentikainen, O. T., Shoji, M., Sasaki, M. *et al.* (2005). Divergent pharmacological activity of novel marine-derived excitatory amino acids on glutamate receptors. *J. Pharmacol. Exp. Ther.* **314**, 1068–1078.
13. Sasaki, M., Maruyama, T., Sakai, R. & Tachibana, K. (1999). Synthesis and biological activity of dysiherbaine model compound. *Tetrahedron Lett.* **40**, 3195–3198.
14. Lomeli, H., Wisden, W., Köhler, M., Keinänen, K., Sommer, B. & Seeburg, P. H. (1992). High-affinity kainate and domoate receptors in rat brain. *FEBS Lett.* **307**, 139–143.
15. Gregor, P., O'Hara, B. F., Yang, X. & Uhl, G. R. (1993). Expression and novel subunit isoforms of glutamate receptor genes GluR5 and GluR6. *NeuroReport*, **4**, 1343–1346.
16. Qiu, C. S., Lash-Van Wyhe, L., Sasaki, M., Sakai, R., Swanson, G. T. & Gereau, R. W., IV (2011). Antinociceptive effects of MSVIII-19, a functional antagonist of the GluK1 kainate receptor. *Pain*, **152**, 1052–1060.
17. Frydenvang, K., Lash, L. L., Naur, P., Postila, P. A., Pickering, D. S., Smith, C. M. *et al.* (2009). Full domain closure of the ligand-binding core of the ionotropic glutamate receptor iGluR5 induced by the high affinity agonist dysiherbaine and the functional antagonist 8,9-dideoxyneodysiherbaine. *J. Biol. Chem.* **284**, 14219–14229.
18. Madden, D. R. (2002). The structure and function of glutamate receptor ion channels. *Nat. Rev., Neurosci.* **3**, 91–101.
19. Armstrong, N., Sun, Y., Chen, G. Q. & Gouaux, E. (1998). Structure of a glutamate-receptor ligand-binding core in complex with kainate. *Nature*, **395**, 913–917.
20. Armstrong, N. & Gouaux, E. (2000). Mechanisms for activation and antagonism of an AMPA-sensitive glutamate receptor: crystal structures of the GluR2 ligand binding core. *Neuron*, **28**, 165–181.
21. Mayer, M. L. (2005). Crystal structures of the GluR5 and GluR6 ligand binding cores: molecular mechanisms underlying kainate receptor selectivity. *Neuron*, **45**, 539–552.
22. Naur, P., Vestergaard, B., Skov, L. K., Egebjerg, J., Gajhede, M. & Kastrup, J. S. (2005). Crystal structure of the kainate receptor GluR5 ligand-binding core in complex with (*S*)-glutamate. *FEBS Lett.* **579**, 1154–1160.
23. Sanders, J. M., Pentikainen, O. T., Settimo, L., Pentikainen, U., Shoji, M., Sasaki, M. *et al.* (2006). Determination of binding site residues responsible for the subunit selectivity of novel marine-derived compounds on kainate receptors. *Mol. Pharmacol.* **69**, 1849–1860.
24. Sommer, B., Burnashev, N., Verdoorn, T. A., Keinanen, K., Sakmann, B. & Seeburg, P. H. (1992). A glutamate receptor channel with high affinity for domoate and kainate. *EMBO J.* **11**, 1651–1656.
25. Hayward, S. & Lee, R. A. (2002). Improvements in the analysis of domain motions in proteins from conformational change: DynDom version 1.50. *J. Mol. Graphics Modell.* **21**, 181–183.
26. Postila, P. A., Swanson, G. T. & Pentikainen, O. T. (2010). Exploring kainate receptor pharmacology using molecular dynamics simulations. *Neuropharmacology*, **58**, 515–527.
27. Birdsey-Benson, A., Gill, A., Henderson, L. P. & Madden, D. R. (2010). Enhanced efficacy without further cleft closure: reevaluating twist as a source of agonist efficacy in AMPA receptors. *J. Neurosci.* **30**, 1463–1470.
28. Swanson, G. T., Green, T. & Heinemann, S. F. (1998). Kainate receptors exhibit differential sensitivities to (*S*)-5-iodowillardiine. *Mol. Pharmacol.* **53**, 942–949.
29. Swanson, G. T., Kamboj, S. K. & Cull-Candy, S. G. (1997). Single-channel properties of recombinant AMPA receptors depend on RNA editing, splice variation, and subunit composition. *J. Neurosci.* **17**, 58–69.

30. Nielsen, M. M., Liljefors, T., Krogsgaard-Larsen, P. & Egebjerg, J. (2003). The selective activation of the glutamate receptor GluR5 by ATPA is controlled by serine 741. *Mol. Pharmacol.* **63**, 19–25.
31. Nanao, M. H., Green, T., Stern-Bach, Y., Heinemann, S. F. & Choe, S. (2005). Structure of the kainate receptor subunit GluR6 agonist-binding domain complexed with domoic acid. *Proc. Natl Acad. Sci. USA*, **102**, 1708–1713.
32. Otwinowski, Z. & Minor, W. (1997). Processing of X-ray diffraction data collected in oscillation mode. *Methods Enzymol.* **276**, 307–326.
33. Brunger, A. T. (2007). Version 1.2 of the crystallography and NMR system. *Nat. Protoc.* **2**, 2728–2733.
34. Brunger, A. T., Adams, P. D., Clore, G. M., DeLano, W. L., Gros, P., Grosse-Kunstleve, R. W. *et al.* (1998). Crystallography & NMR system: a new software suite for macromolecular structure determination. *Acta Crystallogr., Sect. D: Biol. Crystallogr.* **54**, 905–921.
35. Emsley, P. & Cowtan, K. (2004). Coot: model-building tools for molecular graphics. *Acta Crystallogr., Sect. D: Biol. Crystallogr.* **60**, 2126–2132.
36. Steiner, R. A., Lebedev, A. A. & Murshudov, G. N. (2003). Fisher's information in maximum-likelihood macromolecular crystallographic refinement. *Acta Crystallogr., Sect. D: Biol. Crystallogr.* **59**, 2114–2124.
37. Howlin, B., Moss, D. S. & Harris, G. W. (1989). Segmented anisotropic refinement of bovine ribonuclease A by the application of the rigid-body TLS model. *Acta Crystallogr., Sect. A: Found. Crystallogr.* **45**, 851–861.
38. Schuttelkopf, A. W. & van Aalten, D. M. (2004). PRODRG: a tool for high-throughput crystallography of protein–ligand complexes. *Acta Crystallogr., Sect. D: Biol. Crystallogr.* **60**, 1355–1363.
39. Jones, T. A. (1985). Diffraction methods for biological macromolecules. Interactive computer graphics: FRODO. *Methods Enzymol.* **115**, 157–171.

European Journal of Medicinal Chemistry 46 (2011) 2917–2929

Contents lists available at ScienceDirect

European Journal of Medicinal Chemistry

journal homepage: http://www.elsevier.com/locate/ejmech

Original article

Anti-prion activities and drug-like potential of functionalized quinacrine analogs with basic phenyl residues at the 9-amino position

Thuy Nguyen [a], Yuji Sakasegawa [b], Katsumi Doh-ura [b], Mei-Lin Go [a,*]

[a] Department of Pharmacy, Faculty of Science, National University of Singapore, 18 Science Drive 4, Singapore 117543, Singapore
[b] Department of Neurochemistry, Tohoku University Graduate School of Medicine, 2-1 Seiryo-cho, Aoba-ku, Sendai 980-8575, Japan

ARTICLE INFO

Article history:
Received 18 January 2011
Received in revised form
2 April 2011
Accepted 4 April 2011
Available online 12 April 2011

Keywords:
Cell-based anti-prion activity
Quinacrine analogs
Drug-like properties
Binding to human prion protein fragment
PAMPA-BBB permeability
Pgp substrate

ABSTRACT

In this paper, we report the synthesis and cell-based anti-prion activity of quinacrine analogs derived by replacing the basic alkyl side chain of quinacrine with 4-(4-methylpiperazin-1-yl)phenyl, (1-benzylpiperidin-4-yl) and their structural variants. Several promising analogs were found that have a more favorable anti-prion profile than quinacrine in terms of potency and activity across different prion-infected murine cell models. They also exhibited greater binding affinities for a human prion protein fragment ($hPrP_{121-231}$) than quinacrine, and had permeabilities on the PAMPA-BBB assay that fall within the range of CNS permeant candidates. When evaluated on bidirectional assays on a Pgp overexpressing cell line, one analog was less susceptible to Pgp efflux activity compared to quinacrine. Taken together, the results point to an important role for the substituted 9-amino side chain attached to the acridine, tetrahydroacridine and quinoline scaffolds. The nature of this side chain influenced cell-based potency, PAMPA permeability and binding affinity to $hPrP_{121-231}$.

1. Introduction

Prion diseases (transmissible spongiform encephalopathies) are fatal transmissible neurodegenerative disorders that afflict humans and animals alike. Prion pathology and intervention strategies have been extensively reviewed [1–5]. As yet, there is no effective prophylactic or therapeutic agent for these devastating conditions and the prospect of developing a clinical agent remains daunting, primarily due to the unusual biology of the infectious agent (the prion) and the limited understanding of the structure and mechanistic properties of the putative target. According to the "protein only" or prion hypothesis, infectivity resides in an abnormal isoform of the host-encoded cellular prion protein (PrP^{Sc}) which propagates by imposing its conformation onto the normal, non-pathogenic prion protein (PrP^{C}) expressed in host cells [6].

Numerous compounds have shown anti-prion activity in cell culture models of prion disease. These include sulphonated dyes like Congo red, sulphated glycans (dextran sulphate, pentosan polysulphate), and nitrogen heterocycles (chlorpromazine, quinacrine, quinine) among others [3,4]. However, none have demonstrated sufficient activity to halt disease progression in infected animal models [2–4], and the few that were tested in humans at the post-symptomatic stage of the disease, like flupirtine [7], quinacrine [8–11], vidarabine [12], amphotericin B [13], amantadine [14], did not significantly alter the clinical course of the disease. In a patient-preference trial that evaluated the safety and efficacy of the 9-aminoacridine quinacrine in human prion disease (PRION-1) [11], quinacrine did not reverse the course of disease, confirming the findings of earlier reports [9,10]. The lack of efficacy was attributed to inadequate accumulation of quinacrine in the brain, due to its removal by P-glycoprotein (Pgp) which is an efflux protein found in the blood–brain barrier [15]. Indeed, when administered orally to prion-infected mice that were deficient in the genes encoding Pgp, brain levels of quinacrine were significantly increased [15,16]. Intriguingly, in one report [16], quinacrine still failed to extend the survival of prion-infected animals which led the authors to speculate that continuous quinacrine treatment promoted the formation of drug resistant prions. This phenomenon could have contributed to the lack of *in vivo* efficacy of quinacrine and possibly other anti-prion drugs. In spite of its limitations (a Pgp substrate, moderate potency, possible resistance), quinacrine remains a promising lead which on structural modification, has yielded analogs with more potent *in vitro* anti-prion activity. Notable examples are the bis-acridines [17] and quinacrine-imipramine hybrids [18] although the large size (molecular

* Corresponding author. Tel.: +65 6516 2654; fax: +65 6779 1554.
E-mail address: phagoml@nus.edu.sg (M.-L. Go).

0223-5234/$ – see front matter © 2011 Elsevier Masson SAS. All rights reserved.
doi:10.1016/j.ejmech.2011.04.016

weight > 500) and lipophilicity (ClogP > 5) of these potent analogs may hinder their passage across the blood–brain barrier.

In an earlier report, we reported several functionalized monoacridines with anti-prion activities on various prion-infected cell models [19]. Two compounds, an N-(4-methylpiperazinyl)phenylacridine-9-amine (compound 15) and an N-(benzylpiperidinyl) acridine-9-amine (compound 17) (Fig. 1), were particularly outstanding as they reduced or cleared PrP^{Sc} in several cell models at sub-micromolar concentrations that were non-toxic to host cells. Noting that the side chains of these hit compounds have not been associated with anti-prion activity, it is of interest to assess their potential as potent and drug-like fragments with anti-prion activity. To this end, we have prepared analogs of compounds 15 and 17, specifically with modifications at their side chains and evaluated the cell-based anti-prion activities of the resulting compounds. They were also investigated for their binding affinities to a truncated human prion protein ($hPrP_{121–123}$) to provide some insight into their mode of action. Their *in vitro* permeabilities determined by the parallel artificial membrane permeation assay (PAMPA), and susceptibility of a representative compound (**1**) to Pgp efflux were also investigated to gauge the drug-like potential of these target compounds.

2. Chemical considerations

The piperazinylphenyl analog 15 is re-numbered **1** in this report. To investigate the contribution of the 4-methylpiperazine side chain and the substituted acridine ring to anti-prion activity, various analogs were synthesized (Table 1). Modifications to the 4-methylpiperazine ring included replacing the methyl group with its ethyl homolog (**2**), converting the distal basic nitrogen of piperazine to a non-basic amide (**3**) and inserting a methylene (**4**) or carbonyl (**5**) spacer between the piperazine and phenyl rings. The phenyl ring of **1** was replaced by a butynyl-2,3 moiety which is viewed as an aromatic ring equivalent in view of its π-electron density and conformational rigidity [20]. The effect of removing the basic piperazine ring of **1** was investigated in the 9-(N-phenyl) amino analogs **7** and **8**. **8** was additionally modified so that its 9-amino functionality is tertiary. **9** and **10** retained the same 9-amino side chain as **1** but the 2-methoxy-6-chloroacridine ring was replaced by 6-chloro-1,2,3,4-tetrahydroacridine in **9** and 7-chloroquinoline in **10**.

As for the benzylpiperidinyl analog 17, it is re-numbered **11** in this report. The side chain was modified by introducing substituents (*p*-CH_3, *p*-Cl, *p*-OCH_3, *p*-CN) with different Hansch σ and Hammett π values to the phenyl ring (**12**–**15**) and varying the methylene groups ($n = 2$ or 3) separating the piperidine and phenyl rings (**16**–**18**) (Table 1). We also rigidified the piperidine of **11** by converting it to a bicyclic ring (**19**) and switched the positions of the piperidine and phenyl rings found in **11** to give **20**. The tetrahydroacridine and quinoline analogs of **11** were also prepared (**21**, **22**).

1 and its analogs (except **6**, **9**) were synthesized by reacting the appropriate amine and 6,9-dichloro-2-methoxyacridine in refluxing ethanol as solvent [19]. Earlier, we have synthesized **1** by reacting 6,9-dichloro-2-methoxyacridine with 4-(4-methylpiperazin-1-yl) aniline [19]. The aniline was obtained by the Hartwig–Buchwald amination of 1-iodo-4-nitrobenzene with 1-methylpiperazine in the presence of a palladium/BINAP catalyst, followed by catalytic hydrogenation of the nitro group. The same reaction sequence was adopted for the syntheses of 4-(4-ethylpiperazin-1-yl) aniline and 1-[4-(4-aminophenyl)piperazin-1-yl]ethanone which were the reacting amines for **2** and **3** respectively (Scheme 1).

In Scheme 2, commercially available 1-(chloromethyl)-4-nitrobenzene was reacted with 1-methylpiperazine or piperidine in the presence of triethylamine in THF, followed by catalytic reduction of the nitro group with Adam's catalyst. The resulting amines (**25**, **26**) were reacted with 6,9-dichloro-2-methoxyacridine to give **4** and **20** respectively. In a related manner, 4-nitrobenzoyl chloride was reacted with 1-methylpiperazine followed by catalytic reduction to give **27** for the synthesis of **5** (Scheme 3)

2-(4-Chlorobut-2-ynyl)isoindoline-1,3-dione (**28**) was prepared by the Gabriel synthesis of 1,4-dichlorobut-2-yne with potassium phthalimide (Scheme 4) [21]. It was then reacted with 1-methylpiperazine to give **29**, after which the phthalolyl group was removed by hydrazine to give amine **30**. The latter was reacted with 6,9-dichloro-2-methoxyacridine in phenol with heating (120 °C, 4 h) to yield **6**. Aniline and N-methylaniline were reacted with 6,9-dichloro-2-methoxyacridine in refluxing ethanol to give **7** and **8** respectively [19].

3,9-Dichloro-5,6-7,8-tetrahydroacridine (**43**) was synthesized in a one-pot reaction involving 4-chloroanthranilic acid and cyclohexanone [22] (Scheme 5), following which it was reacted with 4-[(4-methylpiperazin-1-yl)methyl]aniline or 1-benzylpiperidin-4-amine in phenol to give **9** and **21** respectively. These amines were also reacted with commercially purchased 4,7-dichloroquinoline to give **10** (refluxing ethanol as solvent) and **22** (phenol as solvent).

11 and its analogs (except **20**) were synthesized by reacting the appropriate amine and 6,9-dichloro-2-methoxyacridine in phenol (120 °C, 4 h) as solvent [19]. 1-Benzylpiperidin-4-amine (for **11**) was purchased while the amines for **12**–**18** were synthesized by reacting *t*-butylpiperidin-4-ylcarbamate with a phenalkyl halide in the presence of triethylamine, to give intermediates **31**–**37**, followed by removal of the protective *t*-Boc moiety by acid hydrolysis to give the desired amine (Scheme 6). The phenalkyl halides were purchased except for 1-chloro-4-(chloromethyl)benzene (**38**) which was obtained by reacting 4-chlorobenzylhydroxy with thionyl chloride in anhydrous dichloromethane.

8-Benzyl-8-aza-bicyclo[3.2.1]oct-3-ylamine (**42**) was synthesized following a reported method [23] with modifications (Scheme 7). Hydrolysis of the ethyl ester of 3-oxo-8-aza-bicyclo [3.2.1]octane-8-carboxylic acid gave the secondary amine (**39**) which was reacted with benzyl chloride to give the ketone **40**. The ketone was derivatized to an oxime **41** and reduced in the presence of Adam's catalyst to give the desired amine **42**. The latter was reacted with 6,9-dichloro-2-methoxyacridine in phenol to give **19**.

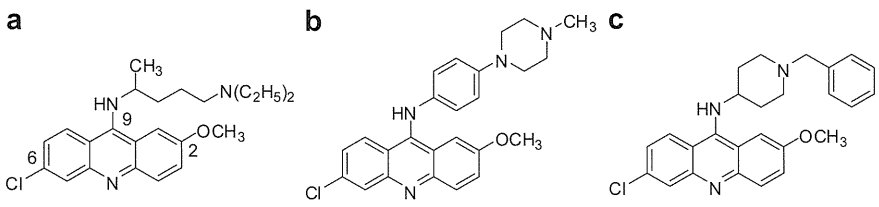

Fig. 1. (a) Quinacrine (b) Compound **15** [19] (c) Compound **17** [19]. In the present report, compounds **15** and **17** are referred to as **1** and **11** respectively.

Table 1
Structures of **1**–**22**.

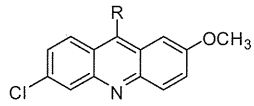

Code	*R*	Code	*R*
1	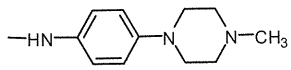	**11**	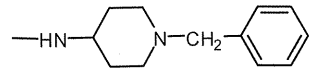
2	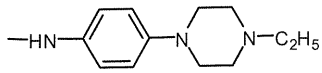	**12**	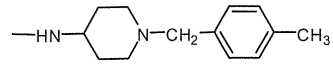
3	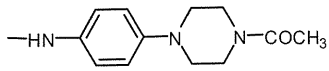	**13**	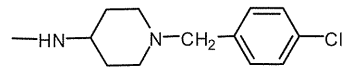
4	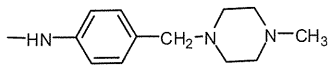	**14**	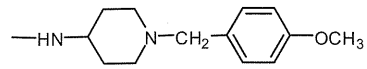
5	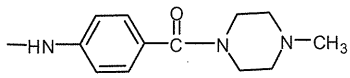	**15**	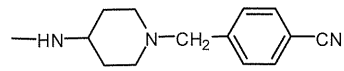
6	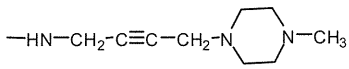	**16**	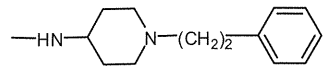
7	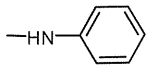	**17**	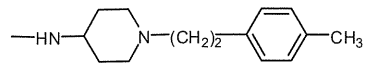
8	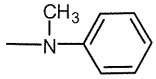	**18**	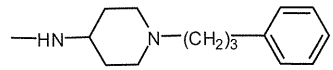
9	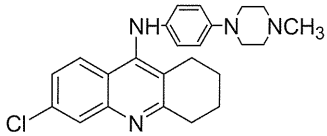	**19**	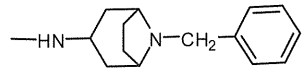
10	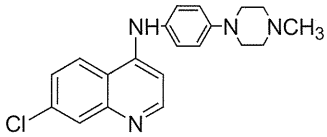	**20**	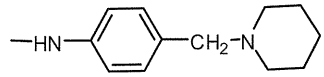
		21	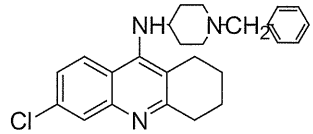
		22	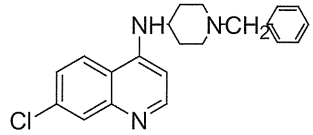

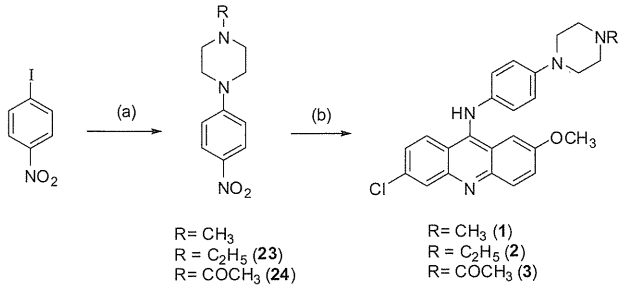

Scheme 1. a) amine, $Pd(OAc)_2$, BINAP, Cs_2CO_3, anhydrous toluene, 120 °C; b) (i) H_2, Pd/C; (ii) 6,9-dichloro-2-methoxyacridine, ethanol, reflux, 24 h.

3. Results

3.1. Anti-prion activity

Anti-prion activity was determined in murine cells that were stably infected with abnormal protease resistant prion protein (PrP^{Sc}) and capable of accumulating PrP^{Sc} in detectable amounts without concurrent cytotoxicity to the host cells. Three prion-infected cell models were investigated, namely ScN2a which comprise mouse neuroblastoma cells (N2a) infected with a mouse adapted scrapie strain (RML), N167 which are N2a cells containing another mouse adapted scrapie strain 22L and F3, a subclone of N2a with higher expression levels of PrP^{C} and infected with the human prion strain Fukuoka-1. Screening for anti-prion activity involved monitoring PrP^{Sc} by Western blotting after proteinase K digestion of cell lysates. A compound with anti-prion activity will show a concentration-dependent reduction in the signal levels of the immunoblots, from which EC_{50} (effective concentration required to reduce PrP^{Sc} content to 50% of untreated cells) is then determined. Besides EC_{50}, the full anti-prion activity (FAA) and maximal tolerant concentration (TC) are also obtained. FAA is the estimated lowest concentration required to clear more than 99% of PrP^{Sc} content, while TC is the approximate highest concentration that has no effect on the viability of infected N2a cells. The screening results are presented in Table 2.

The EC_{50} of the positive control quinacrine on ScN2a was 0.23 μM, which agreed with reported values on a similar cell model [24,25]. It was also active on N167 (EC_{50} 0.59 μM) and F3 (EC_{50} 1.88 μM) but failed to clear PrP^{Sc} at concentrations that did not affect the viability of the host cells. Thus, the target end points required of a compound deemed to have a better anti-prion profile than quinacrine are (i) activity across the three cell models, in particular F3 which has been shown to be resistant to drug treatment [19,26]; (ii) ability to clear PrP^{Sc} in all cell models; and (iii) a high tolerant concentration (TC), preferably exceeding that of quinacrine (TC 2.5 μM). In practical terms, the compound should combine a low EC_{50} with low FAA across several cell models, while maintaining a high TC on uninfected N2a cells. As seen from Table 2, **1** fulfills most of these criteria except that its tolerant concentration remains comparable to that of quinacrine. As for **11**, it fared less well as it failed to clear PrP^{Sc} in F3 and its potency (EC_{50}) did not exceed that of **1** on the existing cell models.

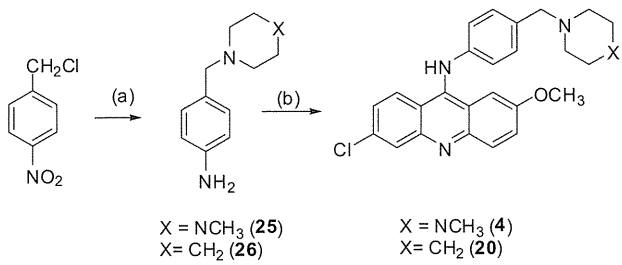

Scheme 2. a) (i) amine, TEA, THF, 70 °C, 24 h; (ii) H_2, PtO_2, 50 psi, overnight; b) 6,9-dichloro-2-methoxyacridine, ethanol, reflux, 24 h.

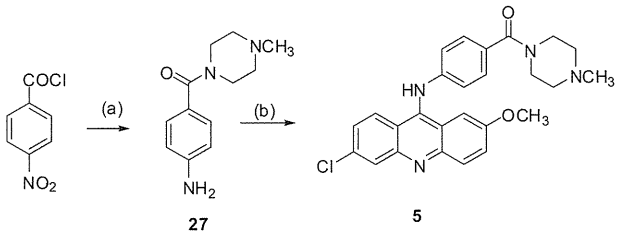

Scheme 3. a) (i) N-Methylpiperazine, TEA, anhydrous DCM, RT, overnight; (ii) H_2, PtO_2, 50 psi, overnight; b) 6,9-dichloro-2-methoxyacridine, phenol, 120 °C, 24 h.

Among the piperazinylphenyl analogs **1**–**10**, several members had lower EC_{50} values than **1** on ScN2a but these improved potencies did not extend to N167 or F3. In fact, only 3 analogs (**4**, **5**, **10**) retained activity on all 3 cell models, but with higher EC_{50} values than **1**. Their lower potencies notwithstanding, these compounds have the advantage of being less toxic (TC 4–12 μM) than **1** and quinacrine.

In spite of the small number of piperazinylphenyl analogs explored here, some broad structure–activity trends may be deduced. First, inserting a spacer moiety (methylene, carbonyl) between the phenyl and piperazine rings retained activity on all 3 cell models. Notably, the analog with the methylene spacer (**4**) exhibited a better anti-prion profile than the carbonyl analog (**5**). Second, homologation of the distal piperazine nitrogen of **1** (4-ethyl in **2** and 4-methylcarbonyl in **3**) adversely affected activity. **2** and **3** are structural isomers of **4** and **5** respectively and their contrasting anti-prion profiles suggest a limited tolerance for even minor modifications to the side chain. Third, the butyn-2,3-yl moiety is a poor substitute for the phenyl ring, as seen from less promising profile of **6**.

We investigated **7** and **8** to determine if a basic substituent on the 9-N-phenyl ring of **1** is essential for activity across the different cell models. The results suggest that the basic substituent contributes to activity. Notably, **7** and **8** had no activity on N167 and F3, but retained potencies on ScN2a (EC_{50} 0.54, 2.51 μM).

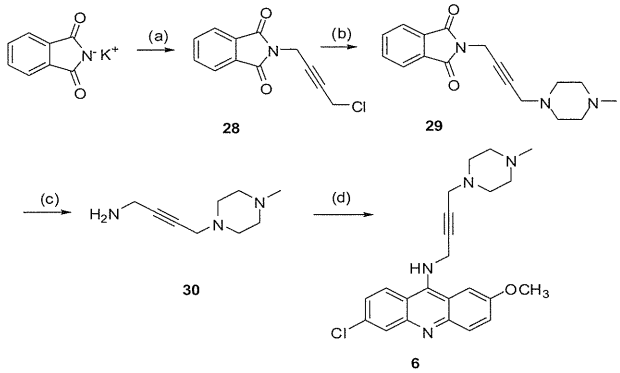

Scheme 4. a) 1,4-dichlorobut-2-yne, DMF, 100 °C, 5 h; b) 1-methylpiperazine, TEA, DCM, rt, overnight; c) NH_2NH_2, EtOH, reflux, 2 h; d) 6,9-dichloro-2-methoxyacridine, phenol, 120 °C, 24 h.

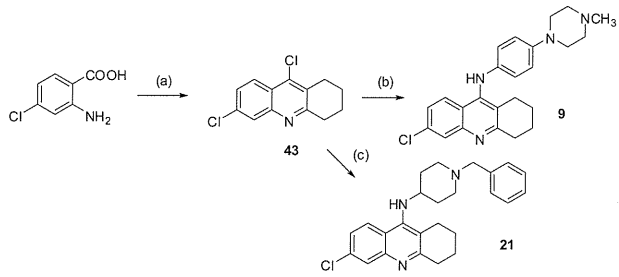

Scheme 5. a) cyclohexanone, $POCl_3$, 0 °C → reflux, 2 h; (b) 4-[(4-methylpiperazin-1-yl)methyl]aniline, ethanol, reflux, 24 h; c) 1-benzylpiperidin-4-amine, phenol, 120 °C, 24 h.

Compound **3** (with a basic substituent) showed a similar profile but was many times more potent on ScN2a (EC_{50} 0.035 μM) than **7** and **8**. Interestingly, we noted that **8** which is the only compound with a tertiary 9-amino functionality, is also the least active analog in Table 2. Earlier, we found that 9-amino-6-chloro-2-methoxyacridine (primary 9-amino function) was as potent as **1** on ScN2a (EC_{50} 0.13 μM) [19] but as seen here, activity declined in **7** (secondary 9-N-phenylamino, EC_{50} 0.54 μM) and even more in **8** (tertiary 9-N-methyl-N-phenylamino, 2.51 μM). Thus, it may be inferred that a tertiary 9-amino function adversely affects anti-prion activity. Lastly, replacing the substituted acridine ring of **1** with tetrahydroacridine (**9**) or quinoline (**10**) reduced activity, particularly on F3, although both analogs were noticeably less toxic (TC ≥ 10 μM) on N2a cells compared to **1**.

Unlike the piperazinylphenyl analogs, more members of the N-benzylpiperidinyl series retained anti-prion activity on all 3 cell models and of these, several are more potent than **11**. The most promising analog is **16** in which the N-benzyl substituent of **11** was replaced by N-phenylethyl. Introducing a *p*-methyl to the N-phenethyl side chain (**17**) or homologation to N-phenpropyl (**18**) are acceptable modifications, but resulted in some loss of potency on F3. Interestingly, a *p*-methyl on the benzyl ring of **11** (**12**) is also permissible, but not substitutents like chloro, methoxy or cyano (**13**–**15**) which do not have the electron donating and lipophilic character of the methyl group. Rigidifying the piperidine ring (**19**) and switching the positions of the phenyl and piperidine rings (**20**) retained activity. **20** is structurally related to **4** and the acceptable activity profiles of both compounds showed that the dibasic piperazine may be replaced by the monobasic piperidine ring. The

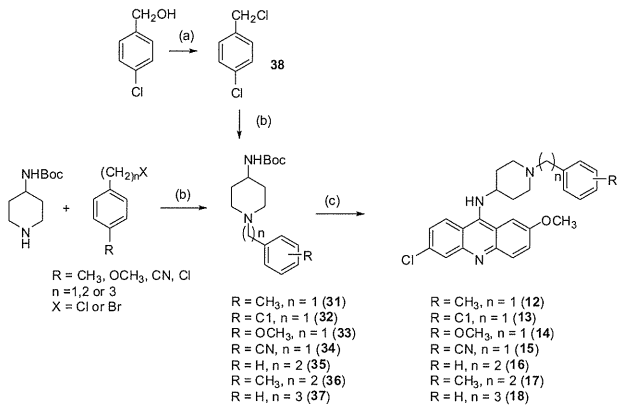

Scheme 6. a) $SOCl_2$, 0 °C → RT, 1 h, anhydrous DCM; b) TEA, THF, reflux, overnight; c) (i) TFA, DCM, rt; (ii) 6,9-dichloro-2-methoxyacridine, phenol, 120 °C, 24 h.

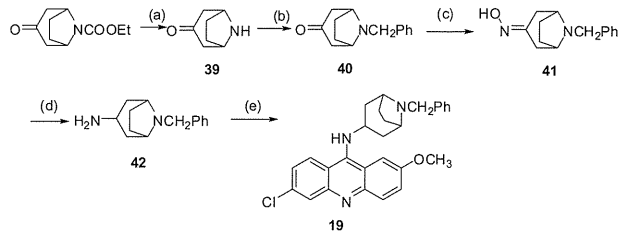

Scheme 7. a) KOH, water, THF, 80 °C, 10 h; b) $PhCH_2Cl$, TEA, THF, reflux, overnight; c) $NH_2OH.HCl$, MeOH, Na_2CO_3, rt, 4 h; d)H_2, PtO_2, 50 psi, rt, overnight; e) dichloro-2-methoxyacridine, phenol, 120 °C, 24 h.

tetrahydroacridine (**21**) and quinoline (**22**) analogs were again associated with lower cytotoxicities but unlike the piperazinylphenyl series, both **21** and **22** were active on ScN2a, N167 and F3. They were also equipotent on F3.

3.2. Binding affinity to truncated human prion protein $hPrP_{121–231}$

The binding affinities of the test compounds to a truncated human prion protein comprising the carboxy-terminal polypeptide residues (121–231) was monitored by surface plasmon resonance (SPR). Briefly, the peptide was immobilized on a carboxymethylated dextran sensor chip (CM5) to give a density of approximately 3000 response units (RU). A known concentration of the test compound was then passed over the chip surface and its binding to the immobilized peptide was monitored by a binding response curve (sensorgram) which showed the rates at which the compound associated and dissociated from the peptide. Fig. 2A is a sensorgram of a typical rapidly associating and dissociating ("fast-on/fast-off") compound (in this case, quinacrine), which is seen from the steep rise and fall of the ascending and descending portions of the plot. The binding capacity of the compound for $hPrP_{121–231}$ is deduced from the maximum response unit (RU_{max}) that is obtained at the end of the association phase and this value is normalized to $\%RU_{max}$ by taking into account the molecular weights of the test compound and peptide, the maximum binding response of the peptide (3000 RU units) and assuming a 1:1 stoichiometry in the interaction. Fig. 2B shows the binding response curve of 9 which is a "slow on/slow off" compound. Dissociation is incomplete as seen from the descending portion of the curve which fails to return to the baseline within the monitoring period.

Some test compounds (**6**, **7** and **19**) were not evaluated because of their poor solubilities in phosphate buffer at the test concentration (50 μM). The remaining compounds interacted with the peptide fragment with a "fast-on/fast-off" profile, except **13** which had a profile that was between that of quinacrine and **9**. The binding parameters of the test compounds are given in Table 3. Also included are the binding affinities of quinacrine and its analogs (**43**–**46**) and 9-amino-6-chloro-2-methoxyacridine (**47**) whose ScN2a EC_{50} values have been reported earlier [19].

Several investigators have measured the binding affinity of quinacrine to prion protein using SPR [27,28]. In spite of differences in the type of protein (mouse or human prion protein, full length or truncated) and concentration (40 μM or 100 μM) used in these assays, the consensus was that quinacrine binds weakly to the prion protein. The classification of compounds as weak or strong binders depends on the experimental conditions employed. Using the carboxy-terminal polypeptide (residues 121–231) of the mouse prion protein immobilized on the CM5 chip, Kawatake et al. [27] classified quinacrine (100 μM) as a weak binder as its RU was <100. Touil et al. [28] screened structurally diverse compounds (40 μM) on

Table 2
In vitro anti-prion activities of **1**–**22** on murine neuroblastoma cells infected mouse adapted scrapie strains (ScN2a and N167) and a human prison strain (F3).

Code	ScN2a		N167		F3		TC (μM)[c]
	EC_{50} (μM)[a]	FAA (μM)[b]	EC_{50} (μM)[a]	FAA (μM)[b]	EC_{50} (μM)[a]	FAA (μM)[b]	
1	0.10 (0.08, 0.12)	0.4	0.42 (0.41, 0.43)	1.5	0.68 (0.59, 0.78)	1.5	2.5
2	0.080, (0.063, 0.10)	1	0.96 (0.43, 2.11)	None[d]	None[d]	ND[e]	3
3	0.035 (0.025, 0.049)	0.1	None[d]	ND[e]	None[d]	ND[e]	5
4	0.060 (0.051, 0.069)	0.5	0.35 (0.22, 0.63)	2	0.86 (0.77, 0.96)	3	4
5	1.23 (1.09, 1.39)	5	4.20 (3.81, 4.63)	7	4.10 (3.49, 4.81)	None[d]	12
6	0.027 (0.021, 0.036)	1	0.99 (0.86, 1.14)	3	None[d]	ND[e]	8
7	0.54 (0.36, 0.81)	None[d]	None[d]	ND[e]	None[d]	ND[e]	5
8	2.51 (2.11, 3.00)	5	None[d]	ND[e]	None[d]	ND[e]	8
9	0.082 (0.058, 0.11)	1	None[d]	ND[e]	None[d]	ND[e]	>10
10	0.14 (0.08, 0.25)	1	0.53 (0.41, 0.68)	2	2.04 (1.35, 3.07)	None[d]	10
11	0.42 (0.38, 0.46)	1	0.49 (0.44 0.55)	1.5	0.80 (0.64, 1.00)	None[d]	2
12	0.15 (0.12, 0.19)	3	0.62 (0.49, 0.80)	1	0.63 (0.53, 0.75)	3	5
13	0.28 (0.24, 0.33)	1	0.34 (0.15, 0.78)	3	None[d]	ND[e]	12
14	0.082 (0.063, 0.11)	1.5	0.52 (0.47, 0.58)	2	None[d]	ND[e]	10
15	0.55 (0.49, 0.63)	1	0.14 (0.081, 0.25)	1	None[d]	ND[e]	5
16	0.13 (0.10, 0.16)	0.5	0.23 (0.12, 0.42)	1	0.19 (0.14, 0.26)	2	2
17	0.076 (0.058, 0.10)	1	0.30 (0.14, 0.66)	1	0.69 (0.39, 1.19)	3	3
18	0.093 (0.027, 0.32)	1	0.32 (0.19, 0.54)	1	1.04(0.77, 1.40)	3	4
19	0.054(0.043, 0.067)	2	0.35 (0.21, 0.61)	1	0.54 (0.48, 0.60)	1.5	2
20	0.099 (0.085, 0.11)	0.5	0.51 (0.24, 1.09)	1	0.64 (0.52, 0.79)	3	5
21	0.54 (0.36, 0.80)	1	0.42 (0.32, 0.57)	3	1.19 (0.85, 1.67)	5	5
22	0.15 (0.13, 0.18)	1	0.23 (0.16, 0.33)	2	1.2 (0.88, 1.64)	3	>10
Quinacrine	0.23 (0.22, 0.25)	0.8	0.59 (0.42, 0.82)	None[d]	1.88 (1.64, 2.16)	None[d]	2.5

[a] Concentration (μM) required to reduce PrP^{Sc} content to 50% of untreated/control cells from 3 independent determinations. 95% confidence limits are given in italics.
[b] Full anti-prion activity (FAA): estimated lowest concentration (μM)to clear more than 99% of PrP^{Sc} content.
[c] Tolerant concentration : approximate highest concentration of test compound that had no effect on viability of murine neuroblastoma N2a cells.
[d] No effect at non-toxic concentration.
[e] Not determined.

human and murine prion proteins immobilized on the same CM5 chip and proposed the following cut-off values, assuming a 1:1 binding mode: multiple site binders >130% RU_{max}, strong binders >50–129% RU_{max} and weak to moderate binders > 5–49% RU_{max}. In that report, % RU_{max} of quinacrine (40 μM) was 36.9% on the truncated human prion protein (residues were not mentioned) and 88.4% on the full length human prion protein. Here, we obtained % RU_{max} of 87.3 for quinacrine (50 μM) using the truncated human prion protein (residues 121–231) on the CM5 chip. We noted that our experimental conditions were closer to that reported by Touil and coworkers [28]. Moreover, our % RU_{max} for quinacrine (87.3) was approximately twice their reported value (36.9). Hence, we adopted their classification for strong/moderate/weak binders but at twice the % RU_{max} cut-off values. Thus, $\%RU_{max}$ for multiple site binders is >260, strong binders 100–259, and weak to moderate binders, <100.

By this criterion, quinacrine is classified as a weak to moderate binder, in line with earlier reports [27,28]. None of the test compounds qualified as multiple site binders. Compounds with the highest binding affinities were the piperazinylphenyl analogs, namely **2** (194), **3** (210), **4** (207) and **5** (232). In comparison, the N-benzylpiperidinyl analogs were generally weaker binders, with a maximum $\%RU_{max}$ value of 174 (**16**). The quinacrine analogs (**43**–**46**) which have dialkylaminoalkyl side chains at 9-amino had $\%RU_{max}$ values (153–178) which qualify them as strong binders, in marked contrast to quinacrine.

A comparison of % RU_{max} and $EC_{50\ ScN2a}$ points to a relationship between binding affinity and potency on ScN2a. For example, the piperazinylphenyl and N-benzylpiperidinyl analogs with the strongest binding affinities were among the more potent anti-prion agents, and interestingly, **8** which had the weakest binding affinity in Table 3, was also the least potent compound on ScN2a. When evaluated by a Spearman bivariate correlation, a significant correlation between the two variables was found, with Spearman rho of −0.470 and p value of 0.018 for the 25 compounds in Table 3. The significant correlation led us to question if there could be a physicochemical basis for the relationship since both affinity and potency measurements were carried out at a pH (7.4) where the compounds were ionized to varying degrees and would have different lipophilicities. Indeed, $\%RU_{max}$ was significantly correlated to the estimated distribution coefficient of the compounds at pH 7.4 (log $D_{7.4}$), with Spearman rho of −0.501, $p = 0.011$ for $n = 25$. The inverse relationship implied that stronger binding affinities were associated with less lipophilic compounds. However, no correlation was observed for $EC_{50\ ScN2a}$ and log $D_{7.4}$.

3.3. Evaluation of permeability by PAMPA-BBB

The permeability characteristics of selected compounds were evaluated on the parallel artificial membrane permeation assay (PAMPA) using porcine brain lipids to mimic the lipid barrier of the brain. This assay which is also referred to as PAMPA-BBB, involved measuring the rate at which the test compound passively diffuses across the lipid layer separating the donor compartment (comprising test compound at 30 or 50 μM in phosphate buffer, pH 7.4) from the acceptor compartment filled with the same buffer solution. The concentration of the test compound was then determined in both compartments to give the effective permeability (P_e). Table 3 lists the P_e values of some piperazinylphenyl and N-benzylpiperidinyl analogs and the reference compounds (positive controls) verapamil, quinidine and caffeine. Verapamil and quinidine are representative "high permeability" (or CNS+) compounds while caffeine represents a low permeability (CNS−) compound. The P_e values of caffeine and verapamil compared favorably with those reported by Di et al. [29] using the same method.

Quinacrine was highly permeable across the lipid barrier with a P_e that was comparable to verapamil. The P_e values of the quinacrine analogs **43**–**46** were also noticeably higher than those of the piperazinylphenyl and N-benzylpiperidinyl analogs. Of the four

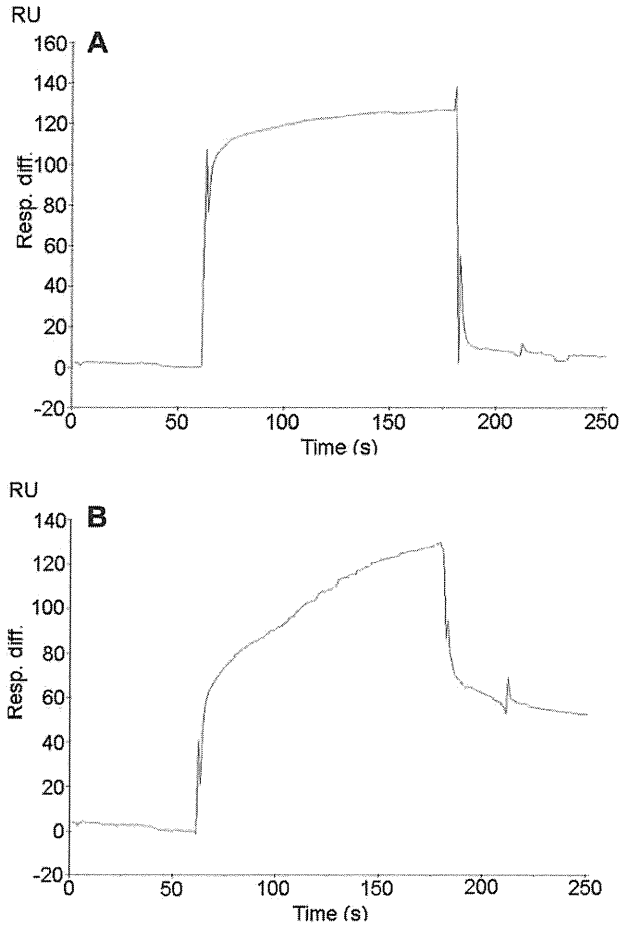

Fig. 2. Interactions of compounds with hPrP121–231 (A) Typical sensorgram of quinacrine, an example of a fast on/fast off compound.(B) Typical sensorgram of 9, a slow on/slow off compounds. Spikes seen at the start and end of injections were due to a slight time delay in the reference cell and appeared when reference subtraction was carried out.

piperazinylphenyl analogs evaluated, P_e ranged from 6.13×10^{-6} cm/s to 11.5×10^{-6} cm/s, with a mean of 8.64×10^{-6} cm/s while P_e of the seven N-benzylpiperidinyl analogs in Table 3 varied from 5.28×10^{-6} cm/s to 15.53×10^{-6} cm/s, with a mean of 8.70×10^{-6} cm/s. Thus, permeabilities of piperazinylphenyl and N-benzylpiperidinyl analogs were broadly comparable but lower than **43**–**46** (mean of 18.17×10^{-6} cm/s). Lower permeabilities notwithstanding, the piperazinylphenyl and N-benzylpiperidinyl analogs are still classified as "CNS+" (high brain penetration) compounds, based on the threshold values proposed by Di and coworkers [29] for "CNS+" ($P_e > 4.0 \times 10^{-6}$ cm/s) and "CNS−" (P_e values $<2.0 \times 10^{-6}$ cm/s) compounds.

The side chains of the piperazinylphenyl and N-benzylpiperidinyl analogs (except **6**) have in common an aromatic residue, a feature that is absent from the dialkylaminoalkyl side chains of quinacrine and its analogs (**43**–**46**). The larger size and lipophilicities of side chains with aromatic residues would influence permeability as noted by others [30]. We found P_e to be inversely correlated to $\log D_{7.4}$ (Spearman rho −0.674, p 0.003, $n = 17$) which meant that lipophilic compounds like the piperazinylphenyl and N-benzylpiperidinyl analogs have lower permeabilities than less lipophilic compounds (**43**–**46**).

3.4. Compound **1** as a substrate of P-glycoprotein (Pgp)

In spite of its favorable permeability and "CNS+" status, accumulation of quinacrine in the brain is hampered by its status as a substrate of the efflux protein P-glycoprotein (Pgp) [15,16,31]. To determine if the Pgp substrate property is still retained in the present series of compounds, we evaluated a representative compound **1** which has good cell-based anti-prion activity (Table 2) and an acceptable P_e value (8.13×10^{-6} cm/s). Briefly, the method involves comparing the bidirectional transport rates of the compound across a layer of Madin–Darby canine kidney (MDCK) cells grown on the insert of a cell culture chamber. The MDCK cells were either parental with normal levels of Pgp (MDCK-WT), or stably transfected with human MDR1 cDNA so that they had higher levels of Pgp (MDCK-MDR1). The rates at which the test compound traverses the cell barrier from the apical (A) to basolateral (B) compartment ($P_{A\rightarrow B}$) and vice-versa ($P_{B\rightarrow A}$) were determined. On normal cells which have constitutional levels of Pgp (MDCK-WT), no significant difference should be detected in the bidirectional transport rates of the test compound even if it is a substrate of Pgp. On the Pgp overexpressing cells (MDCK-MDR1), a Pgp substrate will move across the cells from A→B at a slower rate due to efflux by Pgp which is localized at the apical surface of the cells. In the reverse B→A direction, the Pgp substrate will be transported more rapidly for the same reason. Thus, the efflux ratio ($P_{B\rightarrow A}/P_{A\rightarrow B}$) of a Pgp substrate is generally ≥2 [30] while a non-substrate of Pgp will diffuse across the cell layer at nearly comparable rates ($P_{B\rightarrow A}/P_{A\rightarrow B} \sim 1$). The bidirectional transport rates for **1** and quinacrine across the monolayer of parental and Pgp overexpressing MDCK cells are presented in Table 4.

The efflux ratio of quinacrine on MDCK-WT cells was 1.2, indicating comparable rates of bidirectional transport across this cell barrier. The ratio increased to 5.1 when measured on MDCK-MDR1 cells, which is in keeping with its status as a Pgp substrate. In the case of **1**, the apparent permeability values were noticeably lower (*ca* 10 fold, on both cell lines) than that of quinacrine, indicating slower diffusion rates for **1**. Nonetheless, its efflux ratio on the parental MDCK-WT cells (1.2) was similar to that of quinacrine. On the Pgp overexpressing cells, permeability in the A→B direction was reduced by half (compared to parental cells) but was maintained at similar levels in the B→A direction. Hence, efflux ratio of **1** was only 2.4, suggesting that it may have poorer affinity for Pgp than quinacrine.

Mass balance measurements showed that most of quinacrine and **1** (*ca* >50%) could be accounted in the B→A direction but to a lesser degree in the reverse (A→B) direction. This led us to monitor the degree to which the compounds were retained in the cells and their propensity for adsorption to the experimental set-up. The poor mass balance observed in the A→B direction coincided (in 3 out of 4 instances) with higher levels of cell retention of the test compounds (Table 4). Pgp is asymmetrically expressed in cells, with higher levels found on apical surfaces. Both quinacrine and **1** are weak organic bases and may bind to polyanions like RNA, DNA, ATP or accumulate within acidic intracellular compartments [32]. It may be that the higher protein content of the apical surfaces of these cells predisposed these compounds to be retained in greater amounts.

4. Discussion

In an earlier report, we found that replacing the basic alkyl side chain of quinacrine with aromatic residues bearing basic substituents retained and even improved cell-based anti-prion activity [19]. The most promising analogs were **1** and **11** which had sub-micromolar activities on several prion-infected mouse neuroblastoma cell lines, including the more resistant F3 where host cells were

Table 3
Binding responses of test compounds to hPrP121–231 using surface plasmon resonance, permeability characteristics determined by PAMPA-BBB assay and estimated log *D* at pH 7.4

Code	Binding to hPrP121–231		Permeability parameters from PAMPA-BBB assay	Log $D_{7.4}$[c]
	Binding response (RU_{max})[a,b]	$\%RU_{max}$	Effective permeability P_e ($\times 10^{-6}$ cm/s)[b]	
1	130.2 ± 15.1	120.3	8.13 ± 2.75	3.36
2	184.4 ± 24.1	194.2	6.13 ± 2.03	3.85
3	224.9 ± 1.8	210.0	8.79 ± 0.37	2.73
4	215.0 ± 9.7	207.1	ND[d]	2.35
5	248.1 ± 21.7	231.6	ND[d]	2.75
6	ND[d]	ND[c]	11.52 ± 1.24	2.35
7	ND[d]	ND[c]	ND[d]	3.84
8	35.0 ± 9.5	43.2	ND[d]	5.43
9	113.8 ± 14.4	127.2	ND[d]	4.75
10	125.7 ± 10.3	165.4	ND[d]	3.39
11	67.5 ± 10.3	65.4	ND[d]	3.75
12	85.2 ± 6.6	69.8	ND[d]	4.08
13	94.5 ± 0.3	98.3	15.53 ± 0.85	4.53
14	91.8 ± 18.8	159.8	7.54 ± 2.47	3.60
15	130.0 ± 7.9	109.2	9.15 ± 1.11	3.51
16	169.5 ± 4.0	173.9	7.68 ± 2.69	3.41
17	169.6 ± 1.4	147.5	7.39 ± 1.70	4.15
18	109.6 ± 1.64	114.8	ND[d]	4.12
19	ND[c]	ND[c]	8.31 ± 1.28	2.66
20	162.7 ± 7.1	144.4	5.28 ± 0.34	3.08
21	92.1 ± 7.2	138.2	ND[d]	5.17
22	93.9 ± 19.6	113.7	ND[d]	3.67
Quinacrine	101.5 ± 14.3	87.3	19.30 ± 2.52	1.89
43[e]	115.5 ± 18.1	153.4	20.98 ± 1.01	1.32
44[e]	132.2 ± 3.8	163.6	13.34 ± 2.20	0.96
45[e]	140.2 ± 1.7	162.1	21.98 ± 4.56	1.26
46[e]	174.2 ± 7.3	177.6	16.37 ± 2.89	1.51
47[e]	83.1 ± 17.3	139.0	14.81 ± 4.63	1.97
Quinidine[f]	ND[d]	ND[d]	11.48 ± 1.19	ND[d]
Caffeine[f]	ND[d]	ND[d]	2.46 ± 0.33	ND[d]
Verapamil[f]	ND[d]	ND[d]	18.45 ± 2.26	ND[d]

[a] Binding response was obtained from the maximal response at the end of the association phase from at least 3 experiments on two different chips.
[b] Values are presented as mean ± standard deviation.
[c] Estimated Log *D* at pH 7.4 (ACD/Labs 6.00).
[d] Not determined.
[e] Structures of **43–47**::

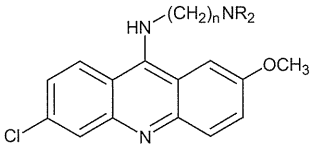

43 n=2, R=C_2H_5

44 : n= 3, R = CH_3

45: n= 3, R=C_2H_5

46: n =4, R = C_2H5

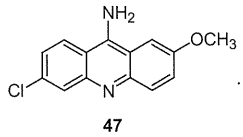

47

[f] Reference compounds for PAMPA-BBB assay. Pe values of caffeine and verapamil were reported to be 1.3 × 10^{-6} cm/s and 16.0 × 10^{-6} cm/s respectively [29].

stably infected with a human prion strain. In this report, **1** and **11** were structurally modified to give a more coherent lead series with the aim of identifying analogs with greater potency and selectivity, while retaining adequate drug-like profiles that would facilitate their passage across the blood–brain barrier.

Of the two hit compounds, **1** was less tolerant of structural modification, as most of the changes explored did not significantly improve anti-prion activity. While the modifications investigated here are admittedly limited in scope and diversity, they do serve to underscore the susceptibility of the scaffold to loss of activity arising from minor changes like homologation (**2–5**) and isosteric replacement (**6**). In contrast, modifying **11** yielded several analogs with improved anti-prion profiles. The most potent analog identified in this investigation is the phenethyl homolog **16** which,

Table 4
Apparent permeability (P_{app}), efflux ratio, mass balance, cell retention and % adsorption onto the Transwell apparatus of Quinacrine and **1** across wild type MDCK-WT and Pgp overexpressing MDCK-MDR1 cell monolayers.

Compound	Cell line	P_{app} ($\times 10^{-6}$ cm/s)[a]		Efflux ratio[b]	Mass balance (%)[a]		Cell retention (%)[a]		Adsorption on Transwell (%)[a]	
		A→B	B→A			B→A	A→B	B→A	A→B	B→A
Quinacrine	MDCK-WT	2.89 ± 0.83	3.45 ± 1.25	1.2	14.6 ± 2.3	51.0 ± 14.4	80.2 ± 9.5	27.7 ± 1.5	5.3 ± 5.0	3.2 ± 2.8
Quinacrine	MDCK-MDR1	1.23 ± 0.05	6.70 ± 1.14	5.1	34.8 ± 10.3	75.8 ± 17.8	35.5 ± 6.2	24.5 ± 7.3	5.5 ± 3.6	3.9 ± 3.1
1	MDCK-WT	0.29 ± 0.04	0.34 ± 0.12	1.2	11.3 ± 1.5	75.3 ± 7.0	66.4 ± 29.0	27.5 ± 12.3	11.4 ± 8.9	3.5 ± 2.5
1	MDCK-MDR1	0.14 ± 0.02	0.34 ± 0.10	2.4	12.6 ± 10.9	73.0 ± 13.9	67.0 ± 14.4	44.2 ± 12.8	6.1 ± 3.7	3.1 ± 2.5

[a] Values were presented as man ± standard deviation from three independent experiments.
[b] Ratio of apparent permeabilities from the basolateral (B) to apical (A) compartment, to that of apical (A) to basolateral (B) compartments. Efflux ratio = P_{app}(B→A)/P_{app}(A→B).

unusual among the other test compounds, was equipotent on both ScN2a and F3 (EC_{50} 0.13 μM, 0.19 μM).

Although the piperazinylphenyl and N-benzylpiperidinyl analogs are distinguished by their N-substituted 9-amino residues, these side chains share common features, namely an aromatic ring and a basic nitrogen-containing heterocycle. The present findings suggest that these features promote, but do not ensure, a broader anti-prion profile. However, in analogs where one but not the other feature is present, the few examples presented here consistently showed no activity on F3 and N167. This was duly observed for **6** and the quinacrine analog **43** [19] (no aromatic ring but with basic moiety) and the piperazinylphenyl analogs **7** and **8** (aromatic ring but without basic moiety).

The acridine ring of **1** and **11** may be replaced by tetrahydroacridine or quinoline. As to whether one scaffold is preferred over the other, the present findings suggest that it is not the scaffold per se, but the side chain attached to it, that influences activity. In this regard, the preferred side chain is the N-(1-benzylpiperidin-4-yl) of **11**, as both the tetrahydroacridine (**21**) and quinoline (**22**) analogs had better anti-prion profiles than the corresponding members with the piperazinylphenyl side chain (**9**, **10**). Potency aside, the ring scaffold has a marked effect on cytotoxicity and analogs with the acridine ring were decidedly more cytotoxic (lower TC) than those bearing other heterocyclic rings.

Many investigators have sought to establish a correlation between EC_{50} derived from cell-based assays and binding affinities to PrP^C as determined from SPR measurements [27,28,33–35]. Compounds that bind to PrP^C are considered more likely to demonstrate an anti-prion effect [28] as the binding step is widely viewed as an important initiating event in prion pathology [1]. Here, we found that $EC_{50\ ScN2a}$ of the test compounds (but not $EC_{50\ F3}$, possibly due to the smaller number of compounds available for analysis) were significantly correlated ($p < 0.05$) to the binding parameters $\%RU_{max}$ and RU_{max}. In this regard, it was of interest to note that the strong binding affinities of the piperazinylphenyl analogs for the truncated prion protein were linked to their lower lipophilicities (log $D_{7.4}$), or more specifically, to the piperazine ring in the side chain. This is demonstrated in **4** and **20**, where replacing the piperazine of **4** with piperidine (**20**) increased $logD_{7.4}$ from 2.35 to 3.08, and concurrently reduced $\%RU_{max}$ from 207 (**4**) to 144 (**20**). As to why a less lipophilic entity is associated with greater binding affinity to PrP^C and by extrapolation, greater anti-prion potency, this question remains to be addressed.

Effective passage across the blood–brain barrier and accumulation in brain tissues are important requirements for anti-prion agents. Quinacrine is known to pass through the blood-brain barrier [36] although accumulation in the brain is curtailed to a significant extent by its efflux by Pgp [15,16,31]. Here we found that the piperazinylphenyl and N-benzylpiperidine analogs had lower PAMPA-BBB permeabilities compared to quinacrine, although their P_e values still qualified them as "high brain penetration" (CNS+) compounds. Like binding affinities, effective permeabilities (P_e) were significantly and inversely correlated to lipophilicities (log $D_{7.4}$). A closer inspection of the correlation showed that the relationship was driven more by the quinacrine analogs (**43**–**46**) rather than the piperazinylphenyl/N-benzylpiperidinyl analogs. The quinacrine analogs had high P_e values (16-22 $\times$ 10^{-6} cm/s) and at least 2-fold magnitude lower lipophilicities (log $D_{7.4}$: 0.96–1.51) than the piperazinylphenyl/N-benzylpiperidinyl analogs. On the other hand, the differences in $logD_{7.4}$ values of the piperazinylphenyl/N-benzylpiperidinyl analogs are no more than a fold magnitude, and probably too narrow in range to differentiate between their permeabilities.

It is apparent that the 9-(N-substituted) side chain strongly influences the anti-prion and physicochemical profiles of the final compound. The non-aromatic and basic side chains of quinacrine and its analogs (**43**–**46**) are largely responsible for their lower lipophilicities and in turn, their strong binding affinities for $hPrP_{123–231}$ and good PAMPA permeabilities. Unfortunately, anti-prion activities were limited to ScN2a and did not extend to other cell models. The aromatic and basic side chains of the piperazinylphenyl/N-benzylpiperidinyl series resulted in more lipophilic compounds, which are strong $hPrP_{123–231}$ binders and still CNS+ in spite of lower PAMPA permeabilities, but with clearly improved cell-based anti-prion profiles.

Although quinacrine has good permeability across the brain, its accumulation is hampered by Pgp which is expressed at high levels at the blood brain barrier. The bidirectional transport of quinacrine on Pgp overexpressing MDCK-MDR1 cells has an efflux ratio of 5, which is in keeping with its status as a Pgp substrate. Interestingly, **1** traversed the MDCK-MDR1 barrier with an efflux ratio that is half that of quinacrine, indicating that it may be a weaker Pgp substrate.

5. Conclusion

Taken together, the present study shows that the piperazinylphenyl and N-benzylpiperidinyl analogs are promising leads for anti-prion design. The 9-N-substituted side chain of these compounds influence anti-prion activity to a significant degree. It also determines the physicochemical profile, in particular lipophilicity and ionizability as assessed from log $D_{7.4}$. Potent and broad ranging anti-prion activities are found in side chains with aromatic residues substituted with basic functionalities. These structural features also diminished effective permeability in PAMPA-BBB by increasing $logD_{7.4}$, but fortunately still kept the compounds within the permeability range of CNS+ compounds. Their lower permeabilities may be compensated by weaker Pgp substrate properties, as found for **1**. If confirmed for other piperazinylphenyl and N-benzylpiperidinyl analogs, this would enhance their standing as potential drug-like and potent anti-prion templates for further investigation.

6. Experimental

6.1. General experimental methods

^1H NMR and ^{13}C NMR spectra were recorded on a Bruker DPX 300 MHz spectrometer and chemical shifts were reported in δ (ppm) relative to the internal standard TMS. Mass spectra (MS, nominal) were collected on an LCQ Finnigan MAT mass spectrometer. Atmospheric pressure ionization (APCI) or electron spray (ionization (ESI)) were used as probes. Reactions were routinely monitored by thin layer chromatography using silica gel 60 F 254 plates from Merck, with UV light as a visualizing agent. Column chromatography was performed using silica gel G (0.04–0.063 mm, Merck). Purity analysis was verified by high-pressure liquid chromatography (HPLC) or by combustion analysis. Combustion analyses (C, H) were determined by Perkin–Elmer PE 2400 CHN/CHNS elemental analyzer by the Department of Chemistry, National University of Singapore. Spectroscopic data, melting points, yields and purities of individual compounds are listed in Appendix 1.

6.2. General procedure for the reaction of 2-methoxy-6,9-dichloroacridine, and 4,7-dichloroquinoline with amines in ethanol as solvent

A previously described method [19] was followed for the syntheses of **1**–**5**, **7**, **8**, **10** and **20**. Briefly, equimolar quantities of the amine and the acridine/quinoline were dissolved in ethanol, 2 drops of conc. HCl were added and the mixture refluxed for

ca 24 h. On cooling, NaOH (1 M) or ammonia solution (25%) was added, followed by dichloromethane to extract the product. Alternatively, if the product precipitated out of solution on alkalinization, it was removed by filtration and purified by column chromatography.

6.3. General procedure for the reaction of 2-methoxy-6,9-dichloroacridine, 3,9-dichloro-5,6,7,8-tetrahydroacridine and 4,7-dichloroquinoline with amines in phenol as solvent

A previously described method [19] was followed for the syntheses of **6**, **9**, **11**–**19**, **21** and **22**. Briefly, equimolar quantities of the amine and the acridine/quinoline were reacted in phenol at 120 °C for 4 h with stirring. On cooling, dichloromethane was added, followed by a solution of NaOH (1 M). The crude product was extracted with dichloromethane and purified by column chromatography.

*6.4. Synthesis of 1-methyl-4-(4-nitrophenyl)piperazine, 1-ethyl-4-(4-nitrophenyl)piperazine (**23**) and 1-[4-(4-nitrophenyl)piperazin-1-yl]ethanone (**24**) by Hartwig-Buchwald amination reaction*

The method of Nguyen Thi et al. was followed [19]. Briefly, Cs_2CO_3, BINAP were added to a flask under argon. A solution of the iodobenzene and amine in dry toluene was added, followed by $Pd(OAc)_2$. The mixture was heated (90 °C) until no trace of the iodobenzene was observed on TLC. On cooling, the reaction mixture was filtered and concentrated to give the crude product which was purified by column chromatography.

6.5. General procedure for catalytic reduction of substituted nitrobenzenes

The substituted nitrobenzenes were reduced to the corresponding anilines by catalytic reduction (50 psi, 10% Pd/C (5% w/w)) on a Parr hydrogenator as previously described [19] The anilines (not characterized) were then condensed with 6,9-dichloro-2-methoxyacridine or 4,7-dichloroquinoline (Section 6.2.) to give **1**–**3**, **10.**

*6.6. Synthesis of 4-[(4-methylpiperazin-1-yl)methyl] benzenamine (**25**) and 4-[(piperidin-1-yl) methyl] benzenamine (**26**)*

These amines were required for the syntheses of **4** and **20** respectively. To a solution of 4-nitrobenzylchloride (1 mmol) in anhydrous THF (3 mL) was added 1-methylpiperazine or piperidine (1 mmol) and triethylamine (1.5 mmol, 0.21 mL). The solution was heated at 70 °C overnight. The reaction mixture was then extracted with dichloromethane and water. The organic fractions were combined, dried over anhydrous Na_2SO_4, and concentrated under reduced pressure. The residue was purified by column chromatography (hexane/EA 1:4) and characterized by ^1H NMR (Supplementary Information). It was dissolved in 10 mL ethanol, PtO_2 (0.01 g) was added under nitrogen. Hydrogenation was carried out on a Parr hydrogenator at 50 psi for 16 h. The catalyst was then removed by filtration and the filtrate was concentrated in vacuo to give the amine in quantitative yield.

*6.7. (4-Aminophenyl) (4-methylpiperazin-1-yl) methanone (**27**)*

This amine was required for the synthesis of **5**. 4-nitrobenzoylchloride (1 mmol, 0.186 g) in anhydrous dichloromethane (5 mL) was reacted with 1-methylpiperazine (1 mmol, 0.11 mL) and triethylamine (1.5 mmol, 0.21 mL) overnight with stirring at room temperature. Workup was carried out as described in Section 6.6 to give 0.249 g of (4-methylpiperazin-1-yl) (4-nitrophenyl) methanone, yellow liquid. ^1H NMR (300 MHz, $CDCl_3$) δ 2.33 (s, 3H), 2.40 (m, 2H), 2.51 (m, 2H), 3.39 (m, 2H), 3.82 (m, 2H), 7.57 (d, J = 8.6, 2H), 8.28 (d, J = 8.6, 2H). MS(ESI) m/z [M + H^+] 250.1. Reduction to give the title compound was carried out as described in Section 6.6.

*6.8. Synthesis of 4-(4-methylpiperazin-1-yl) but-2-yn-1-amine (**30**) [21]*

1,4-Dichloro-2-butyne (6 mmol, 0.58 mL) was added to the stirred suspension of potassium phthalimide (3 mmol, 0.556 g) in DMF (5 mL), and heated to 100 °C for 5 h. After cooling, the reaction mixture was extracted with dichloromethane and water. The organic layers were pooled, dried, and concentrated in vacuo. The residue was purified by column chromatography (hexane/ethyl acetate 1:19) to furnish 0.35 g of 2-(4-chlorobut-2-ynyl)isoindoline-1,3-dione (**28**) (white solid, yield 50%). ^1H NMR (300 MHz, $CDCl_3$) 4.11 (s, 2H), 4.51 (s, 2H), 7.75 (dd, $J1$ = 3.1, $J2$ = 5.5, 2H), 7.89 (dd, $J1$ = 3.1, $J2$ = 5.4, 2H). ^{13}C NMR (75 MHz, $CDCl_3$) δ 27.1, 45.7, 46.9, 51.7 (2C), 54.7 (2C), 78.1, 78.4, 123.4 (2C), 131.9 (2C), 134.0 (2C), 166.9 (2C). **28** was reacted with 1-methylpiperazine following the method described in Section 6.6. to give 2-(4-(4-methylpiperazin-1-yl)but-2-ynyl)isoindoline-1,3-dione (**29**): Yellow solid, 83% yield. ^1H NMR (300 MHz, $CDCl_3$) δ 2.28 (s, 3H), 2.45 (m, 4H), 2.58 (m, 4H), 3.26 (s, 2H), 4.47 (s, 2H), 7.73 (dd, $J1$ = 3.1, $J2$ = 5.4, 2H), 7.88 (dd, $J1$ = 3.1, $J2$ = 5.4, 2H). MS(APCI) m/z [M + H^+] 298.2. A solution of **29** (0.72 mmol, 0.213 g) and hydrazine (0.72 mmol, 0.03 mL) in 1 mL of ethanol was heated at reflux for 2 h. After cooling to 0 °C, phthalhydrazide was removed by filtration. Evaporation of the filtrate gave **30** as a free base. ^1H NMR (300 MHz, $CDCl_3$) δ 2.30 (s, 3H), 2.49–2.61 (m, 8H), 3.28 (t, J = 1.8, 2H), 3.44 (t, J = 1.8, 2H). ^{13}C NMR (75 MHz, $CDCl_3$) δ 29.7, 31.6, 46.0, 47.2, 52.0 (2C), 53.0, 54.9 (2C). MS(ESI) m/z [M + H^+] 168.1.

6.9. General method for the synthesis of 1-benzylpiperidine-4-amine, 1-phenethylpiperidine-4-amine, 1-phenpropylpiperidine-4-amine and their ring substituted analogs

A solution of piperidin-4-yl carbamic acid t-butyl ester (2 mmol), phenylalkyl halide (2 mmol), and triethylamine (6 mmol) in tetrahydrofuran (THF, 5 mL) was refluxed overnight, THF was removed in vacuo, dichloromethane was added and the mixture was extracted with dilute $NaHCO_3$. The organic fractions were combined, dried over anhydrous Na_2SO_4, concentrated in vacuo, and the residue purified by column chromatography (EA/hexane) to give the carbamic acid t-butyl ester intermediates (**31**, **33**–**37**) (Supplementary Information). In the case of t-butyl 1-(4-chlorobenzyl)piperidin-4-ylcarbamate (**32**), 1-chloro-4-(chloromethyl) benzene (**38**) was synthesized by adding $SOCl_2$ (15 mmol, 1.1 mL) dropwise at 0 °C to a stirred solution of 4-chlorobenzylhydroxy (5 mmol, 0.713 g) in anhydrous dichloromethane (5 mL). The reaction mixture was allowed to reach room temperature, stirred for 1 h, and then cooled down to 0 °C again. It was then carefully diluted with water, and neutralized with saturated $NaHCO_3$. The reaction mixture was extracted with dichloromethane and washed with water to afford the product **38** as a yellow oil (0.64 g, 80%) (Supplementary Information).

The carbamic acid tert-butyl ester intermediate was dissolved in dichloromethane (4 mL) and tetrafluoroacetic acid (TFA, 4 mL) was added dropwise. The reaction mixture was neutralized with saturated (5 M) NaOH, extracted with dichloromethane and $NaHCO_3$ solution to give the desired amine as an oil. The amine was not characterized but reacted immediately with 6,9-dichloro-2-methoxyacridine by the general procedure described in Section 6.3.

6.10. Synthesis of 8-benzyl-8-aza-bicyclo[3.2.1]octan-3-amine (**42**) [23]

A solution of ethyl 3-oxo-8-azabicylo[3.2.1]octane-8-carboxylic acid (2.3 mmol, 0.46 g) in ethanol (1 ml) was mixed with KOH (0.353 g) in water (5 mL) and heated at 100 °C for 3 h. After cooling down to room temperature, the solution was diluted with 20 mL of dichloromethane. The organic layer was dried and concentrated in vacuo to give crude 8-aza-bicyclo[3.2.1]octan-3-one (**39**). ^{1}H NMR (300 MHz, $CDCl_3$) δ 1.69 (m, 2H), 1.90 (dd, $J1 = 4.1$, $J2 = 8.8$, 2H), 2.31 (m, 1H), 2.36 (m, 2H), 2.56 (m, 2H), 3.87 (m, 2H). ^{13}C NMR (75 MHz, $CDCl_3$) δ 30.0 (2C), 50.8 (2C), 54.9 (2C), 209.7. **39** was reacted with benzyl chloride as in Section 6.6 to give 8-benzyl-8-aza-bicyclo [3.2.1]octan-3-one (**40**). ^{1}H NMR (300 MHz, $CDCl_3$) δ 1.63 (m, 2H), 2.16 (m, 4H), 2.72 (m, 2H), 3.50 (m, 2H), 3.76 (m, 2H), 7.34 (m, 5H). ^{13}C NMR (75 MHz, $CDCl_3$) δ 27.7 (2C), 48.1 (2C), 55.1, 58.6 (2C), 127.2, 128.4 (2C), 128.5 (2C), 138.9, 210.1. MS(APCI) *m/z* [M^+] 215.3. To obtain the oxime **41**, hydroxylamine hydrochloride (1.7 mmol, 0.117 g) was stirred in methanol (7 mL) at 0 °C. The slurry was treated with Na_2CO_3 (0.09 g) and stirred for 5 min after which **40** (1.36 mmol, 0.29 g) in methanol (1 mL) was added. After stirring for 5 h at room temperature, methanol was removed in vacuo, the residue was treated with dichloromethane and brine, the organic fractions were combined, dried (anhydrous Na_2SO_4), and concentrated to give 0.2 g of the oxime **41** as a white solid (Yield 65%). ^{1}H NMR (300 MHz, $CDCl_3$) δ 1.52 (t, $J = 9.6$, 1H), 1.63 (t, $J = 9.6$, 1H), 2.04 (m, 2H), 2.14 (d, $J = 14.7$, 1H), 2.26 (dd, $J1 = 2.7$, $J2 = 12.6$), 2.62 (d, $J = 14.7$, 1H), 2.99 (d, $J = 15.6$, 1H), 3.36 (b, 2H), 3.66 (s, 2H), 7.25–7.42 (m, 5H). ^{13}C NMR (75 MHz, $CDCl_3$) δ 26.6, 27.5, 31.3, 37.1, 55.5, 57.8, 58.4, 127.0, 128.2 (2C), 128.7 (2C), 138.9, 156.3. MS(ESI) *m/z* [$M + H^+$] 231.1. The oxime **41** was reduced with Adam's catalyst as described in Section 6.6 to give the title compound **42** as a yellow oil (76%) which was not characterized and reacted immediately to give **19** (Section 6.3).

6.11. 3,9-Dichloro-5,6,7,8-tetrahydroacridine (**43**) [22]

To a mixture of 2-amino-4-chlorobenzoic acid (5 mmol, 0.858 g) and cyclohexanone (5 mmol, 0.52 mL) was carefully added 5 mL of $POCl_3$ at 0 °C. The mixture was heated under reflux for 2 h, then cooled to room temperature, and concentrated to give a slurry. The residue was diluted with dichloromethane, neutralized with aqueous K_2CO_3, and washed with brine. The organic layer was dried over anhydrous Na_2SO_4 and concentrated in vacuo to furnish 1.12 g of **43** as a reddish brown solid (Yield 88%). ^{1}H NMR (300 MHz, $CDCl_3$) δ 1.89 (m, 4H), 2.88 (t, $J = 5.3$, 2H), 3.06 (9t, $J = 5.3$, 2H), 7.34 (dd, $J1 = 1.9$, $J2 = 8.9$, 1H), 7.89 (m, 2H). ^{13}C NMR (75 MHz, $CDCl_3$) δ 22.1, 22.2, 27.1, 33.4, 123.3, 124.7, 126.8, 127.1, 128.9, 135.1, 141.4, 145.9, 160.5. MS(APCI) *m/z* [M^+] 252.7.

6.12. Evaluation of cell-based anti-prion activity

The anti-prion activity of test compounds was determined on ScN2a, N167 and F3 cell models as described by Nguyen Thi et al. [19].

6.13. Preparation of human prion protein 121–231 ($hPrP_{121-231}$)

Recombinant PrP (rPrP, human PrP 121-231aa with an N-terminal histidine tag and Factor Xa digestion sequence) was bacterially expressed as inclusion bodies by the *Escherichia coli* protein expression pET system. The inclusion bodies were solubilized in 8 M urea, 25 mM Tris–HCl, 300 mM NaCl, pH 7.5 and then purified by metal chelating chromatography (HiTrap-Ni, GE Health Science). The purified rPrP was refolded by rapid dilution and incubation in 1 M arginine–HCl, 1 mM oxidized glutathione, pH 8.0 at 37 °C overnight. The refolded rPrP was dialyzed against water and concentrated by centrifugal membrane (Amicon Ultra-15, MWCO 3000, Millipore). To remove N-terminal histidine tag, rPrP (0.2 mg/mL) was digested with 0.3 μg/mL trypsin at 16 °C for 16 h in 25 mM Tris–HCl, pH 7.5. The N-terminal histidine tag-truncated rPrP was purified by anion-exchange chromatography (UNO-Q, 1 mL, Bio-Rad), buffer was changed to 10 mM NaOAc (pH6.0) with Amicon Ultra-15, and stored at −80 °C. Protein concentration was determined by UV measurement and found to be equivalent to 0.79 mg/ml.

6.14. Evaluation of binding affinity by surface plasmon resonance

The assay was performed on a BIAacore 3000 platform (BIAcore, Uppsala, Sweden) following reported methods with modifications [27,28]. The sensor chip CM5 and amine coupling kit were purchased from GE Healthcare Bio-sciences AB (Uppsala, Sweden). The running buffer was prepared by filtering and degassing a phosphate buffer 1×, pH 7.4 containing 2.5% DMSO. Recombinant human prion protein (amino acids 121–231; hPrP121–231, molecular weight 12,544.97 Da) was dissolved in 10 mM sodium acetate buffer, pH 4.5 (10 μg/ml) and immobilized on the CM5 chip to reach a density of *ca* 3000 response units (RU) using amine coupling. A reference surface was prepared by treating a blank flow cell in the same way as the flow cell containing the immobilized peptide. Stock solutions of test compounds (2 mM) were prepared in DMSO and diluted to 50 μM with phosphate buffer 1×, pH 7.4. Each analytical cycle consisted of running buffer for 60 s (stabilization phase), a sample injection of 50 μM in running buffer for 120 s (association phase) and running buffer for 150 s (dissociation phase). Flow rates were kept at 30 μL/min. Surface regeneration of the chip was carried out by injecting 10 mM NaOH (30 s, flow rate of 30 μL/min). After regeneration, the surface was allowed to stabilize for *ca* 60 s before the next injection. The binding response curve was obtained by subtracting the background signal (from the reference flow cell) from that of the sample flow cell in order to correct for non-specific binding and bulk effects due to the analyte. The binding affinity was taken as the maximum response at the end of the association phase as seen from the binding response curve. Binding was expressed as % RU_{max} which is defined as the % theoretical maximum binding response units (RU) and determined by the following equation assuming a 1:1 stoichiometry:

$$\%RU_{max} = \left[RU_{compound}/RU_{immobilized\ protein}\right] \times \left[MW_{protein}/MW_{compound}\right] \times 100\%$$

6.15. Evaluation of permeability by the PAMPA-BBB assay

The method described by Di et al. [29] was followed with modifications. Porcine polar brain lipid (PBL) (catalog no. 141101) was purchased from Avanti Polar Lipids, Inc. (Alabaster, Alabama, USA). Dodecane was obtained from Sigma–Aldrich. The acceptor plate was a 96-well filter plate (MultiscreenTM-IP, catalog no. MAIPN4510, PVDF membrane, pore size is 0.45 μm) from Millipore (Bredford, USA) and the donor plate was a 96-well plate (catalog no. MATRNPS50, Millipore, Billerica, MA, USA). The 96-well UV plate (catalog no. 3535) was purchased from Corning Inc. (NY, USA). Compounds were dissolved in DMSO at 10 mM, and diluted in phosphate buffer solution 1×, pH 7.4–50 μM or 30 μM depending on their aqueous solubilities. An aliquot (300 μL) of the diluted solution was transferred to the donor well. The filter membrane was coated with 5 μL of 20 mg/mL PBL in dodecane and the

acceptor well was filled with 150 μL of the same phosphate buffer solution. The donor plate was carefully aligned to the acceptor plate such that the underside of the membrane remained in contact with buffer solution in the donor wells. The sandwich assemble was incubated in an airtight humid box at room temperature for 10 h. The concentrations of compound in the acceptor, donor and reference wells were determined by UV absorbance at 270 nm using the Tecan Infinite 200 microplate reader. Permeability rate (Pe_e) and membrane retention (R) were calculated using the following equations:

$$P_e = -\frac{2.303V_A}{A \cdot t}\left[\frac{1}{1+r_v}\right]\log_{10}\left\{1 - \left[\frac{1+r_v^{-1}}{1-R}\right]\frac{C_A(t)}{C_D(t=0)}\right\}$$

$$R = 1 - \frac{V_A C_A(t) + V_D C_D(t)}{V_D C_D(t=0)}$$

where A is the active surface area of membrane (0.24 cm^2), t is the incubation time (s), V_A and V_D are the volumes (cm^3) of the acceptor and donor chambers, $r_v = V_D/V_A$, C_A and C_D are drug concentrations in the acceptor and donor chambers.

6.16. Cell-based bidirectional transport assay

Dulbeco's Modified Eagle's medium (DMEM) was purchased from Sigma (MO, USA). Fetal bovine serum was from Hyclone Lab Inc. (Logan, UT, USA). The MDCK-WT (wild type) and MDCK-MDR1 (overexpressing Pgp) were gifts from Dr. Piet Borst (Netherlands Cancer Institute, University of Amsterdam, Netherlands). Western blotting was performed on these two cell lines to confirm the overexpression of Pgp as described [37]. Transwell® plates (Cat. no 3401, 12 mm diameter, 0.4 μm pore size) were obtained from Costar Corp. (Cambridge, MA, USA). The Millicell-ERS system was from Millipore Corp. (Bedford, MA, USA). Transport medium was Hank's balance salt solution (HBSS) from Invitrogen (CA, USA) supplemented with 10 mM HEPES at pH 7.4 (HBSS–HEPES). 10 mM stock solutions of quinacrine and **1** were prepared in DMSO and further diluted to 10 μM with the transport medium (HBSS–HEPES). The MDCK-MDR1 cell line was grown in DMEM supplemented with 10% fetal bovine serum, 100 mg/L penicillin, and 100 mg/L streptomycin at 37 °C in an atmosphere containing 5% CO_2. For transport assay, cells with passage number 3–8 were seeded at a density of 300,000 cells/well and grown for 4 days in 12-well Transwell® plates. Cell monolayers with transepithelial electrical resistance (TEER) values greater from 120 to 150 Ω cm^2 were used for the experiment. On the day of assay, fresh medium was added to the cells. Two hours later, they were washed twice and equilibrated with HBSS-HEPES medium for 30 min 500 μL of 10 μM test compounds was added to the apical chamber and 1500 μl of HBSS–HEPES was dispensed to the basolateral chamber for determining apical to basolateral (A→B) transport. After 2 h, cells were lysed with 600 μL of lysis solution (acetonitrile:water:formic acid = 70:30:0.1) for 10 min and the cell debris removed by centrifugation (12,000g, 5 min, 4 °C). Both chambers were thoroughly washed with 1 ml of the same lysis solution and this wash solution was tested for presence of compounds adsorbing onto the plastic surface of the Transwell apparatus. Similarly, 500 μL of HBSS–HEPES was introduced to the apical chamber and 1500 μL of the test solution to the basolateral chamber to determine the basolateral to apical (B→A) transport. Aliquots (10 μL) were withdrawn from each chamber for quantification by LC/MS/MS (Supplementary Information). The integrity of the monolayer was determined by TEER value and by monitoring the transport of Lucifer yellow, a fluorescent marker for paracellular transport. TEER value was calculated using the following equation:

$$\text{TEER} = \left(R_{\text{cell layer}} - R_{\text{blank}}\right) \times A$$

where $R_{\text{cell layer}}$ = Resistance (Ω) of the cell molaye, R_{blank} = Resistance (Ω) of the blank (insert without cells), A = Effective surface area of the insert (1 cm^2 for the 12-well insert).

Cell layers with TEER values in the range of 120–150 Ω cm^2 were deemed suitable for the bidirectional assay. Apparent permeability (P_{app}, cm/s) was calculated as:

$$P_{app} = J/C_0 = [V_r \cdot C_r]/[A \cdot t \cdot C_0]$$

where J is the flux rate, C_0 is the initial concentration in the donor compartment, V_r is the volume of the receiver compartment at the end of the assay, C_r is concentration of compound in the receiver compartment at the end of the assay, A is the effective surface area of the insert, t is duration of the assay (2 h). Mass balance was determined as

$$MB(\%) = [C_{At} \cdot V_A + C_{Bt} \cdot V_B]/[C_0 V_D] \times 100\%$$

where C_{At} is the concentration of compound in the apical compartment at the end of the assay, V_A is volume of the apical compartment, C_{Bt} is the concentration of compound in the basal compartment at the end of the assay, C_0 is the initial concentration in the donor compartment, V_D is the volume of the donor compartment.

6.17. Statistical analysis

Spearman correlation analysis was carried out using SPSS version 13.0. (SPSS Inc., IL, USA). Log D at pH 7.4 was determined with ACD/Labs 6.00 (Advanced Chemistry Development, ON, CN).

Acknowledgments

The authors gratefully acknowledged support by National University of Singapore (NUS) Academic research Fund R148000064112 (to GML) and the Program for the Promotion of Fundamental Studies in Health Science of the NIBIO in Japan, and by the Health and Labor Sciences Research Grant (Research on Measures for Intractable Diseases) from the Ministry of Health, Labor, and Welfare of Japan (to KD and YS). TN was supported by the NUS Ministry of Education Research Scholarship for her graduate studies.

Appendix. Supplementary data

Supplementary data related to this article can be found online at doi:10.1016/j.ejmech.2011.04.016.

References

[1] A. Aguzzi, A.M. Calella, Prions: protein aggregation and infectious diseases, Physiol. Rev. 89 (2009) 1105–1152.
[2] C.R. Trevitt, J. Collinge, A systematic review of prion therapeutics in experimental models, Brain 129 (2006) 2241–2265.
[3] V.L. Sim, B. Caughey, Recent advances in prion chemotherapeutics, Infect. Disord. Drug Targets 9 (2009) 81–91.
[4] K. Teruya, K. Kawagoe, T. Kimura, C.J. Chen, Y. Sakasegawa, K. Doh-ura, Amyloidophilic compounds for prion diseases, Infect. Disord. Drug Targets 9 (2009) 15–22.
[5] G. Mallucci, J. Collinge, Rational targeting for prion therapeutics, Nat. Rev. Neurosci. 6 (2005) 23–34.
[6] S.B. Prusiner, Novel proteinacious infectious particles cause scrapie, Science 216 (1982) 136–144.
[7] M. Otto, L. Cepek, P. Ratzka, Efficacy of flupirtine on cognitive function in patients with CJD: a double-blind study, Neurology 62 (2004) 714–718.
[8] S. Haik, J.P. Brandel, D. Salomon, Compassionate use of quinacrine in Creutzfeldt–Jakob disease fails to show significant effects, Neurology 63 (2004) 2413–2415.